

Hunting for Planetary Nebulae toward the Galactic Center

JIHYE HONG,¹ JANET P. SIMPSON,² DEOKKEUN AN,³ ANGELA S. COTERA,² AND SOLANGE V. RAMÍREZ⁴

¹*Department of Science Education, Ewha Womans University, 52 Ewhayeodae-gil, Seodaemun-gu, Seoul 03760, Republic of Korea; deokkeun@ewha.ac.kr*

²*SETI Institute, 189 Bernardo Avenue, Mountain View, CA 94043, USA*

³*Department of Science Education, Ewha Womans University, 52 Ewhayeodae-gil, Seodaemun-gu, Seoul 03760, Korea; deokkeun@ewha.ac.kr*

⁴*Carnegie Observatory, 813 Santa Barbara Street, Pasadena, CA 91101, USA*

ABSTRACT

We present near-infrared (IR) spectra of two planetary nebula (PN) candidates in close lines of sight toward the Galactic center (GC) using the Gemini Near-Infrared Spectrograph (GNIRS) at Gemini North. High-resolution images from radio continuum and narrow-band IR observations reveal ringlike or barrel-shaped morphologies of these objects, and their mid-IR spectra from the *Spitzer* Space Telescope exhibit rich emission lines from highly-excited species such as [S IV], [Ne III], [Ne V], and [O IV]. We also derive elemental abundances using the Cloudy synthetic models, and find an excess amount of the *s*-process element Krypton in both targets, which supports their nature as PN. We estimate foreground extinction toward each object using near-IR hydrogen recombination lines, and find significant visual extinctions ($A_V > 20$). The distances inferred from the size versus surface brightness relation of other PNe are 9.0 ± 1.6 kpc and 7.6 ± 1.6 kpc for SSTGC 580183 and SSTGC 588220, respectively. These observed properties along with abundance patterns and their close proximity to Sgr A* (projected distances $\lesssim 20$ pc) make it highly probable that these objects are the first confirmed PN objects in the nuclear stellar disk. The apparent scarcity of such objects resembles the extremely low rate of PN formation in old stellar systems, but is in line with the current rate of the sustained star formation activity in the Central Molecular Zone.

Keywords: Planetary nebulae(1249), Milky Way Galaxy(1054), Interstellar Line Emission(844), Galactic center(565)

1. INTRODUCTION

Most stars with initial masses less than $\sim 8 M_\odot$ evolve into planetary nebulae (PNe) at the end of their lifetimes (see Balick & Frank 2002, and references therein), as long as their progenitor masses are large enough (see Jacoby et al. 1997). In our Galaxy, a large number of PNe ($\sim 3,500$) have been discovered so far, many of which are associated with the Galactic bulge or thin disk (e.g., Parker et al. 2006; Miszalski et al. 2008; Jacoby et al. 2010; Sabin et al. 2014), serving as bright tracers for kinematics (e.g., Durand et al. 1998; Beaulieu et al. 2000) and chemical abundance studies in the Milky Way (e.g., Stanghellini & Haywood 2018). However, it has been known for a while that this number is an order of magnitude lower than expected from population synthesis models (e.g., Moe & De Marco 2006), and the majority of PN populations in the Milky Way remain to be discovered. The heavy dust obscuration near the Galactic plane is likely the main cause of such dis-

crepancy (e.g., Jacoby & Steene 2004; Miszalski et al. 2008; Parker et al. 2012).

In this context, the absence of PNe in the nuclear bulge of the Milky Way (Serabyn & Morris 1996; Launhardt et al. 2002) can be understood to be the result of the large amount of foreground dust toward the Galactic center (GC; $A_V \sim 30$), which essentially prohibits detections and identifications of PNe through the conventional method of measuring optical emission lines. The mass of the nuclear bulge is $\sim 1.4 \times 10^9 M_\odot$ (Launhardt et al. 2002), which is approximately 10 times less massive than the kiloparsec-scale classical bulge. The stellar populations in the nuclear bulge are predominantly old (e.g., Nogueras-Lara et al. 2020), but may have distinct chemical properties from the classical bulge (e.g., Schultheis et al. 2020). Most of these stars are confined to the nuclear stellar disk, a rotating disk of stars around Sgr A*. The nuclear stellar disk spatially overlaps with the Central Molecular

Zone (CMZ; see [Morris & Serabyn 1996](#), and references therein), a massive reservoir of molecular gas clouds with a diameter of ~ 500 pc and a total cloud mass of $\sim 3\text{--}8 \times 10^7 M_\odot$ ([Dahmen et al. 1998](#); [Tsuboi et al. 1999](#)). Sustained star formation activity is observed throughout the region (e.g., [An et al. 2011](#); [Longmore et al. 2013](#)). Given that both the Galactic bulge and thin disk harbor a noticeable number of PNe, the lack of PNe in the nuclear bulge poses a challenge to our understanding of PN formation, stellar populations, and evolution in the innermost region of the Milky Way.

Recently, we have identified two objects, SSTGC 580183 (G359.9627-0.1202) and SSTGC 588220 (G0.0967-0.0511), as candidate PNe ([Simpson 2018](#)) while analyzing mid-infrared (IR) spectra of compact IR sources toward the CMZ ([An et al. 2009, 2011](#)). They show high-excitation lines such as [Na III] $7.3 \mu\text{m}$, [Ne V] $14.3 \mu\text{m}$ and $24.3 \mu\text{m}$, and [O IV] $25.9 \mu\text{m}$. These lines are not observed in typical H II regions, but are often seen in PNe with an extremely hot ($3 \times 10^4 \lesssim T_{\text{eff}} \lesssim 2 \times 10^5$ K) central object (e.g., [Osterbrock & Ferland 2006](#); [Peimbert et al. 2017](#)). The two objects have also been observed in high-resolution radio observations and with near-IR narrowband filters, revealing a ringlike or barrel-shaped nebulosity ([Wang et al. 2010](#); [Zhao et al. 2020](#)).

In this paper, we report near-IR spectroscopic follow-up observations of these two objects using the Gemini Near-Infrared Spectrograph (GNIRS; [Elias et al. 2006a,b](#)) at the Frederick C. Gillett Gemini North Telescope. Owing to a paucity of PNe toward the GC, both objects are unique, providing an opportunity to explore stellar evolution and chemical characteristics of stellar populations in the inner region of the Galaxy. Their probable location in the CMZ is an interesting aspect of this study, since the massive reservoir of molecular gas in the CMZ is known to maintain the most intense star-forming activity in the Milky Way ($\sim 0.1 M_\odot \text{ yr}^{-1}$; [An et al. 2011](#); [Longmore et al. 2013](#)); they can be used to study chemical and kinematical properties of stars that are distinct from those of other Galactic components.

The primary goal of this study is to confirm the nature of these nebular sources as PNe and to characterize their chemical properties based on near-IR and mid-IR spectra. The near-IR spectra are particularly useful for this purpose, because hydrogen recombination lines can be used to constrain foreground extinction, which is necessary to derive the elemental abundances of ionic species from mid-IR spectra. This paper is organized as follows. In § 2, we describe the observing tactics and data reduction. In § 3, we present the GNIRS spectra, derive fore-

ground extinction from hydrogen recombination lines, and put a constraint on their distances from a comparison with size versus surface brightness relations of PNe. We conduct a joint analysis of near-IR and mid-IR spectra in § 4 to derive elemental abundances. A summary of the work is provided in § 5.

2. OBSERVATIONS AND DATA REDUCTION

2.1. Candidates

Both SSTGC 580183 ($\alpha = 17\text{h } 46\text{m } 0.034\text{s}$, $\delta = -29^\circ 1' 50.210''$) and SSTGC 588220 ($\alpha = 17\text{h } 46\text{m } 2.984\text{s}$, $\delta = -28^\circ 52' 45.320''$) were originally identified as compact (within a $2''$ beam) sources in *Spitzer* Space Telescope ([Werner et al. 2004](#)) Infrared Array Camera (IRAC; [Fazio et al. 2004](#)) images ([Ramírez et al. 2008](#)). They were targeted for follow-up observation using the Infrared Spectrograph (IRS; [Houck et al. 2004](#)) on board *Spitzer* ([An et al. 2009, 2011](#)), as part of a search for massive young stellar objects in the CMZ. There are no parallax measurements, but their proximity to the GC (with a projected angular distance of $\sim 7'$) is deemed as a supporting piece of evidence for their potential membership in the CMZ, which covers a region of $\sim 3^\circ \times 0.5^\circ$ centered at the GC.

Figure 1 shows mid-IR spectra of each target, taken using the high-resolution modules of IRS (see [An et al. 2009, 2011](#), for more details). The background emission from surrounding clouds in the CMZ was subtracted from the spectrum of each target using a set of background spectra (see below). The continuum of the background spectra is characterized by warm-dust emission and strong emission from polycyclic aromatic hydrocarbons at 6.2 , 7.7 , 11.3 , 12.7 , and $16.4 \mu\text{m}$; nonetheless, they are $\sim 2\text{--}3$ times fainter than the target spectrum in the short-high (SH) module ($10 \mu\text{m} \lesssim \lambda \lesssim 20 \mu\text{m}$), and $\sim 5\text{--}8$ times fainter in the long-high (LH) module ($20 \mu\text{m} \lesssim \lambda \lesssim 30 \mu\text{m}$). There are also a number of strong emission lines seen in the background spectra, which originate from diffuse ionized gas and photodissociation regions (PDRs) in molecular clouds adjacent to each target.

The mean background spectrum of the high-resolution modules was constructed using IRS observations at four carefully chosen locations ($\sim 1'$ away in each direction) with the same instrument setup. Figure 2 shows the emission lines observed in the IRS spectra after the background subtraction (see [An et al. 2011](#), for more information on the IRS observations). The strong PDR emission lines from H_2 S(2) 12.28 and H_2 S(1) $17.04 \mu\text{m}$ are negligible after the background subtraction. On the other hand, while some forbidden emission lines from highly-excited ion species such as [S IV] 10.51 and [O IV]

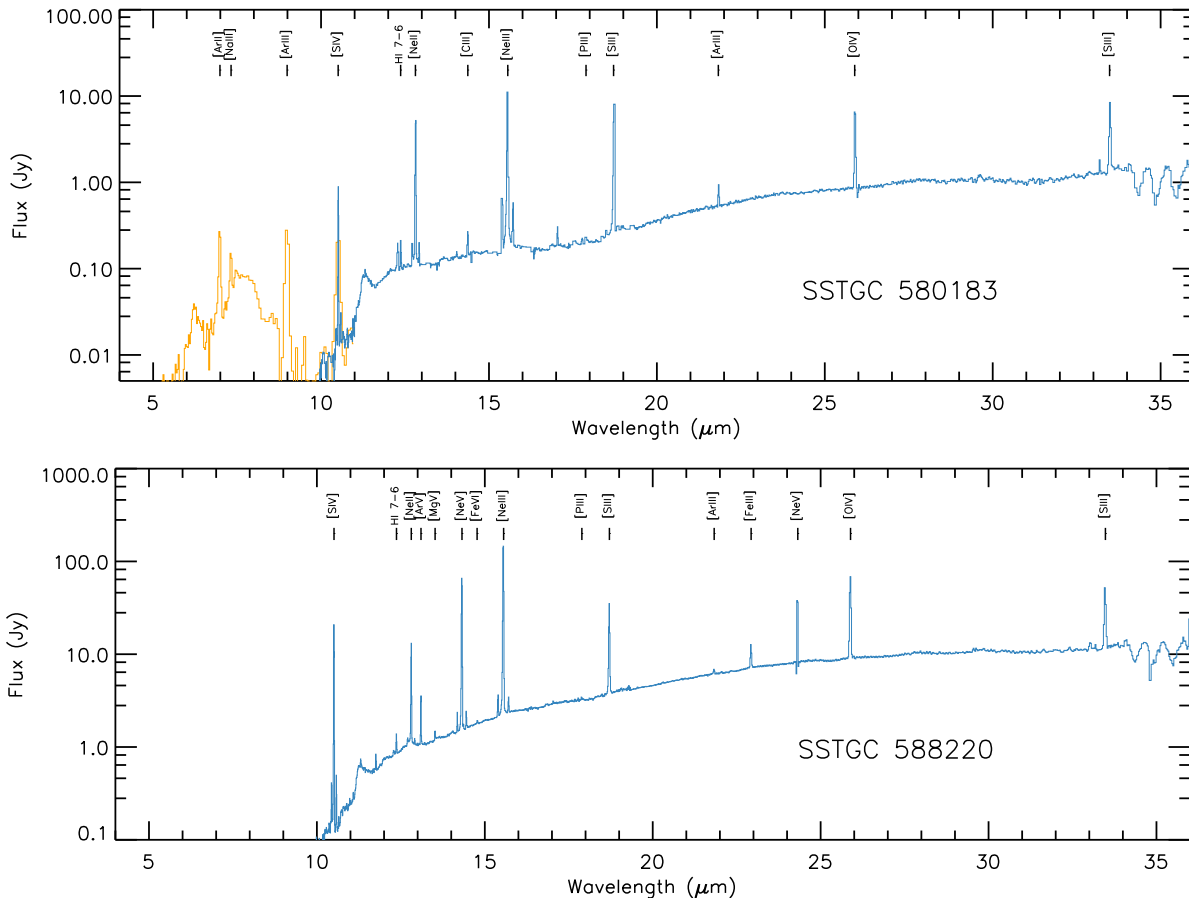


Figure 1. Background-subtracted *Spitzer*/IRS spectra of PN candidates. Spectra from high-resolution modules are shown by blue lines. For SSTGC 580183, low-resolution spectra are displayed by orange lines.

25.89 μm are not visible or are very weak in the background spectra, they are clearly seen in the background-subtracted spectra.¹ SSTGC 588220 additionally exhibits emission from [Ar V] 13.10 μm , [Mg V] 13.52 μm , and [Fe VI] 14.77 μm . Such lines are commonly observed in PNe from gas ionized by a source of temperature $\sim 10^5$ K, rather than from typical H II regions ionized by massive OB stars (e.g., [Osterbrock & Ferland 2006](#)).

2.2. Gemini/GNIRS Observations

Medium-resolution ($R \sim 2600$) near-IR (1.05 μm to 2.22 μm) spectra of the two PN candidates were taken using Gemini/GNIRS. A $0.675'' \times 7''$ slit with the 110.5 mm^{-1} grating was used in cross-dispersed (XD) mode with the short-blue camera (0.15'' per pixel); the slit width was set to approximately match the seeing during the observation. Both targets were observed in queue

observing runs; SSTGC 580183 was observed twice, on 2016 March 11 and April 16, with the former observation taken with a nonzero parallactic angle. In the following analysis, we used averaged line fluxes from both observations, but took only the March data at short wavelengths ($\lambda < 2 \mu\text{m}$), because no such emission lines were detected in the latter data set. SSTGC 588220 was observed on 2016 March 19. The sky was mostly clear and the seeing was stable (0.5''–0.7'') during the observations.

Figure 3 displays locations of GNIRS slits for SSTGC 580183, overlaid on top of the UKIRT Infrared Deep Sky Survey (UKIDSS; [Lawrence et al. 2007](#)) *K*-band image (top panel) and a Jansky Very Large Array (JVLA) 5.5 GHz radio image ([Zhao et al. 2020](#), bottom). This object was not resolved in earlier radio observations ([Yusef-Zadeh et al. 2004](#); [Mills et al. 2011](#)), but the higher-resolution image in [Zhao et al. \(2020\)](#) clearly reveals a ringlike structure with a diameter of $\sim 4''$ along the major axis. The GNIRS slit was put nearly at the center of the ring.

¹ [O IV] 25.89 μm is saturated in the high-resolution IRS spectrum of SSTGC 588220, for which we used the low-resolution IRS spectrum in the modeling (see below).

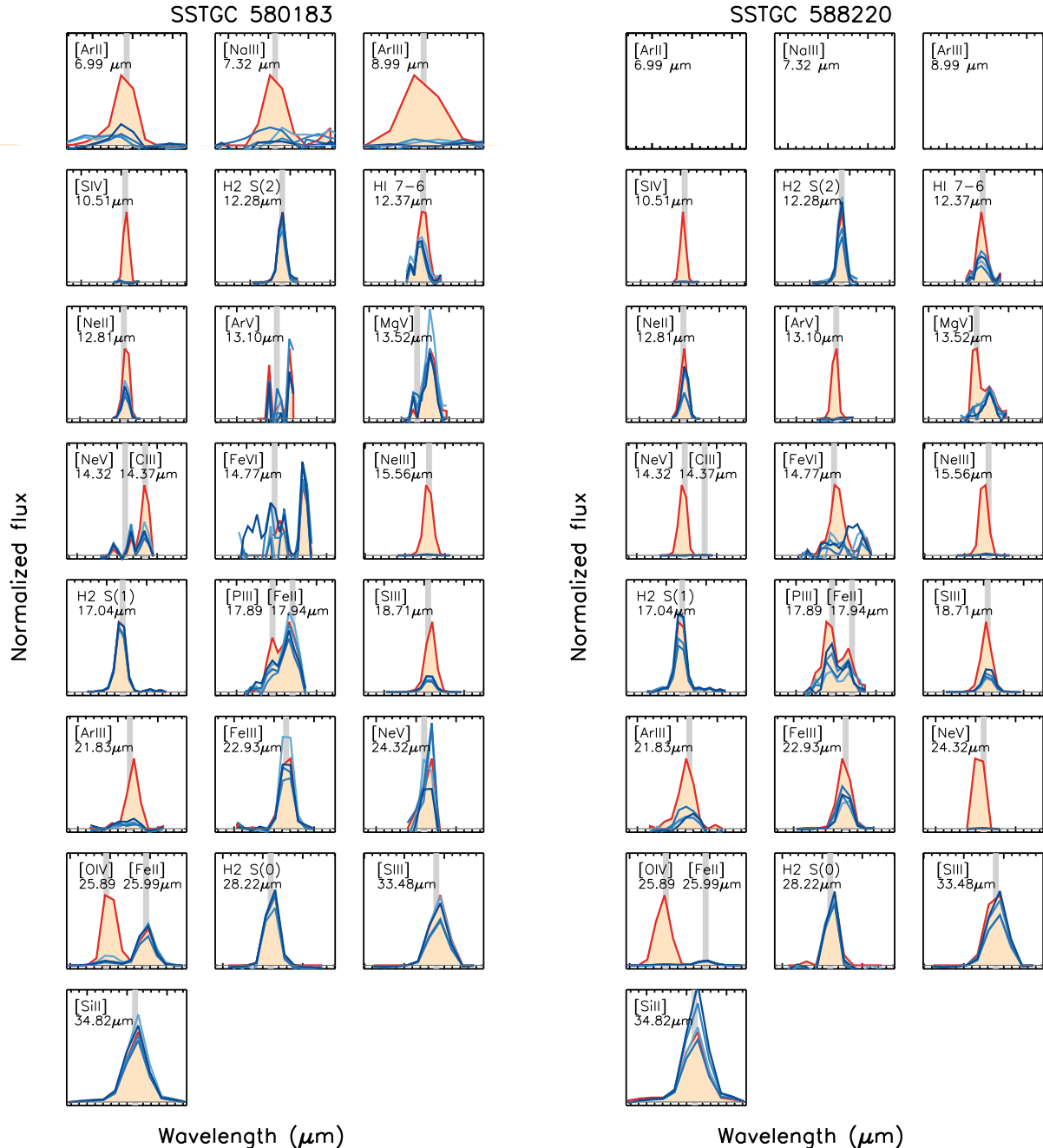


Figure 2. Emission lines in the *Spitzer*/IRS spectra of the PN candidates. Original line emissions from each target are shown by the orange-shaded red lines, while the blue lines show emission lines extracted at four nearby locations that do not contain bright point sources in the slit. Line centers are marked by a vertical gray stripe. Each panel spans a wavelength range of $0.3 \mu\text{m}$ (each tick mark covers $\Delta\lambda = 0.02 \mu\text{m}$).

Previously, SSTGC 588220 was observed in a Paschen- α imaging survey using the *Hubble Space Telescope* (Wang et al. 2010). As displayed in Figure 4, the high-resolution ($\sim 0.2''$) image reveals a bright central region with a diameter of $\sim 2''$ and a fainter elongated ring that extends $\sim 3''$ from the center along the north-south direction. According to the morphological classification of PNe in Sahai et al. (2011), the object can be classified

as having a pair of collimated lobes (L class; the fainter, elongated ringlike structure) with a barrel-shaped central region (brr(o) subclass). Numerical simulations in Akashi et al. (2018) suggest that such barrel-like PNe can be formed through interactions of circumstellar material with jets in a binary system. As shown by the long rectangular box in Figure 4, we put the GNIRS slit in a way that the center of the slit pass through the eastern

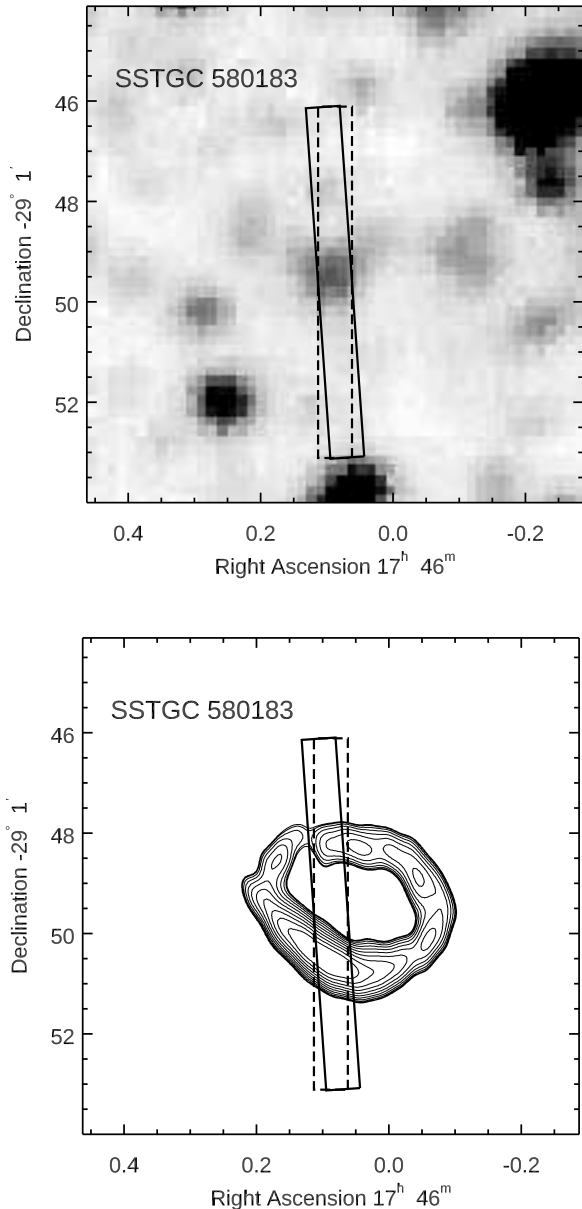


Figure 3. The UKIDSS K -band image (Lawrence et al. 2007, top) and the JVLA 5.5 GHz contour plot (Zhao et al. 2020, bottom) of SSTGC 580183. The GNIRS slit is overlaid on top of each image. The dashed and solid lines indicate the slit position/angle on 2016 March 11 and 2016 April 16, respectively. North is to the top, and east to the left.

part of the barrel-shaped central region. The position angle at the time of observation was set to the parallactic angle; fortuitously, a part of the northern (fainter) lobe was also observed and included in the following analysis.

Because of the high source density in the GC, the off-source slit position was carefully chosen near each target, and a background spectrum was obtained in an

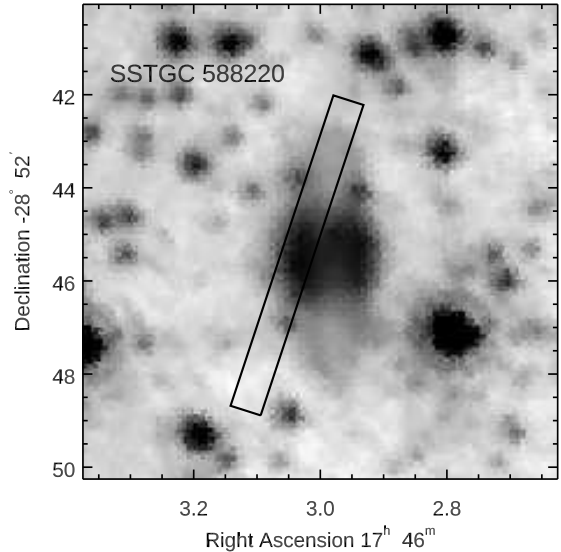


Figure 4. *HST*/NICMOS Paschen α (F187) image (Wang et al. 2010) of SSTGC 588220. North is to the top, and east to the left. The long rectangle indicates the location of the slit on 2016 March 19.

on-off sequence. The total on-source exposure time was 300 s each night. We began reducing the GNIRS data by removing pattern noise and performing flat-field correction using the Gemini IRAF packages². For each set of data frames, we adjusted bias levels by matching the median values of pixels between spectral orders. We then followed the standard data reduction procedure for GNIRS³ to correct for order distortion, and perform wavelength calibration using an argon lamp.

Figure 5 shows source profiles along the slit. For SSTGC 580183 (top panel), a striking bimodal structure is seen in the line emission profiles; we attribute this to the ringlike morphology (R class in Sahai et al. 2011) observed in the radio image (see the bottom panel of Figure 3). The bimodal structures in strong lines, such as Br γ and H I 7–4 (2.166 μ m), are similar, and are also seen in weaker lines, although to a lesser degree. To collect light from the entire line emission structure, we used a 4.2''-wide aperture for spectral extraction.

On the other hand, SSTGC 588220 (middle and bottom panels of Figure 5) shows a single peak, although the slit contains extended emission and its dispersion is larger than the seeing (FWHM \sim 0.6''–0.7''). Most

² IRAF is distributed by the National Optical Astronomy Observatory, which is operated by the Association of Universities for Research in Astronomy (AURA) under a cooperative agreement with the National Science Foundation.

³ <https://www.gemini.edu/instrumentation/gnirs/data-reduction>

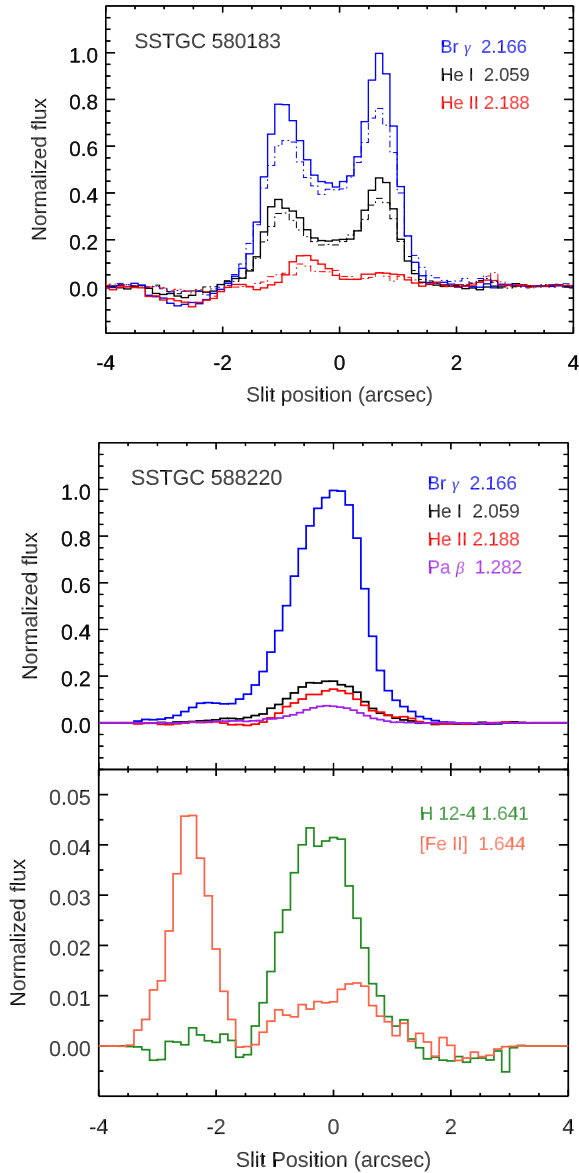


Figure 5. The flux distribution of individual lines along the slit for SSTGC 580183 (top) and SSTGC 588220 (middle and bottom). Line fluxes summed over 6 \AA are normalized with respect to the maximum value of $\text{Br } \gamma$ emission. The dotted-dashed and solid lines in the top panel show the line fluxes from the first and second runs on the target, respectively. North is to the left.

notably, $[\text{Fe II}] 1.644 \text{ \mu m}$ from SSTGC 588220 is significantly brighter in the northern lobe, and is displaced by $\sim 2.5''$ from the central emission (bottom panel). Other lines also show emission at the location of the northern lobe, but its strength is significantly weaker than the one observed in the slit center. We used a $3.6''$ aperture to extract the spectra, collecting both the central emission and the emission from the northern lobe. For $[\text{Fe II}]$,

Table 1. Line Flux Measurements from GNIRS Spectra

Line	Wavelength (μm)	Flux ($10^{-15} \text{ erg s}^{-1} \text{ cm}^{-2}$)	
		SSTGC 580183	SSTGC 588220
He I	1.0833	< 0.256	5.311 ± 0.078
Pa β	1.2822	< 0.256	6.423 ± 0.099
Br 12-4	1.6412	< 0.256	1.405 ± 0.038
$[\text{Fe II}]$	1.6440	< 0.256	1.049 ± 0.212
H_2 1-0 S(2)	2.0338	< 0.256	0.201 ± 0.045
He I	2.0587	6.140 ± 0.389	10.413 ± 0.057
He I	2.1128	0.387 ± 0.020	1.178 ± 0.051
He I	2.1137	< 0.256	0.663 ± 0.223
H_2 1-0 S(1)	2.1218	0.145 ± 0.059	0.738 ± 0.045
He I	2.1615	< 0.256	0.719 ± 0.049
He I	2.1649	0.626 ± 0.041	2.339 ± 0.201
Br γ	2.1661	8.370 ± 0.395	31.395 ± 0.443
He II	2.1884	0.252 ± 0.022	3.143 ± 0.044
$[\text{Kr III}]$	2.1990	0.249 ± 0.112	0.403 ± 0.037
$\langle v_r^{\text{helio}} \rangle$		$+62 \pm 2 \text{ km s}^{-1}$	$-160 \pm 9 \text{ km s}^{-1}$
$\langle v_r^{\text{LSR}} \rangle$		$+72 \pm 2 \text{ km s}^{-1}$	$-150 \pm 9 \text{ km s}^{-1}$

NOTE—Fluxes with 1σ uncertainties are shown. Upper limits are indicated as 3σ detection limits.

the emission line spectrum was extracted at the place where the line emission was strongest. We corrected for telluric absorptions using Spextool v4.1 (Cushing et al. 2004), based on nightly observations of the telluric standard star (HD 157918).

3. RESULTS

3.1. Line Flux Measurements

Our GNIRS spectra of SSTGC 580183 and SSTGC 588220 are shown in Figures 6 and 7, respectively. The observed spectra contain several hydrogen and helium recombination lines, as well as $[\text{Fe II}] 1.644 \text{ \mu m}$, $[\text{Kr III}] 2.199 \text{ \mu m}$, H_2 1-0 S(1) 2.1218 \mu m , and S(2) 2.0338 \mu m . Among these, $\text{Br } \gamma$ (2.166 \mu m) and $\text{Pa } \beta$ (1.282 \mu m) are of particular importance in this study, since they provide a strong constraint on the amount of foreground extinction toward each object. For SSTGC 580183, only the K -band spectrum from the longest wavelength order is shown, because most lines are essentially undetected (see individual panels at the bottom). Even $[\text{Fe II}]$ shows a possible absorption feature, which might reflect the widespread $[\text{Fe II}]$ emission from the interstellar medium (ISM) around the source (see An et al. 2013; Simpson 2018). $\text{Pa } \beta$ was detected at 2.5σ in March, but it was not seen in the April data due to a slightly lower signal-to-noise ratio (S/N). The weak $\text{Pa } \beta$ is indicative of a large foreground extinction (see below).

Table 1 contains the line fluxes measured from the GNIRS spectra. They were measured by fitting a Gaus-

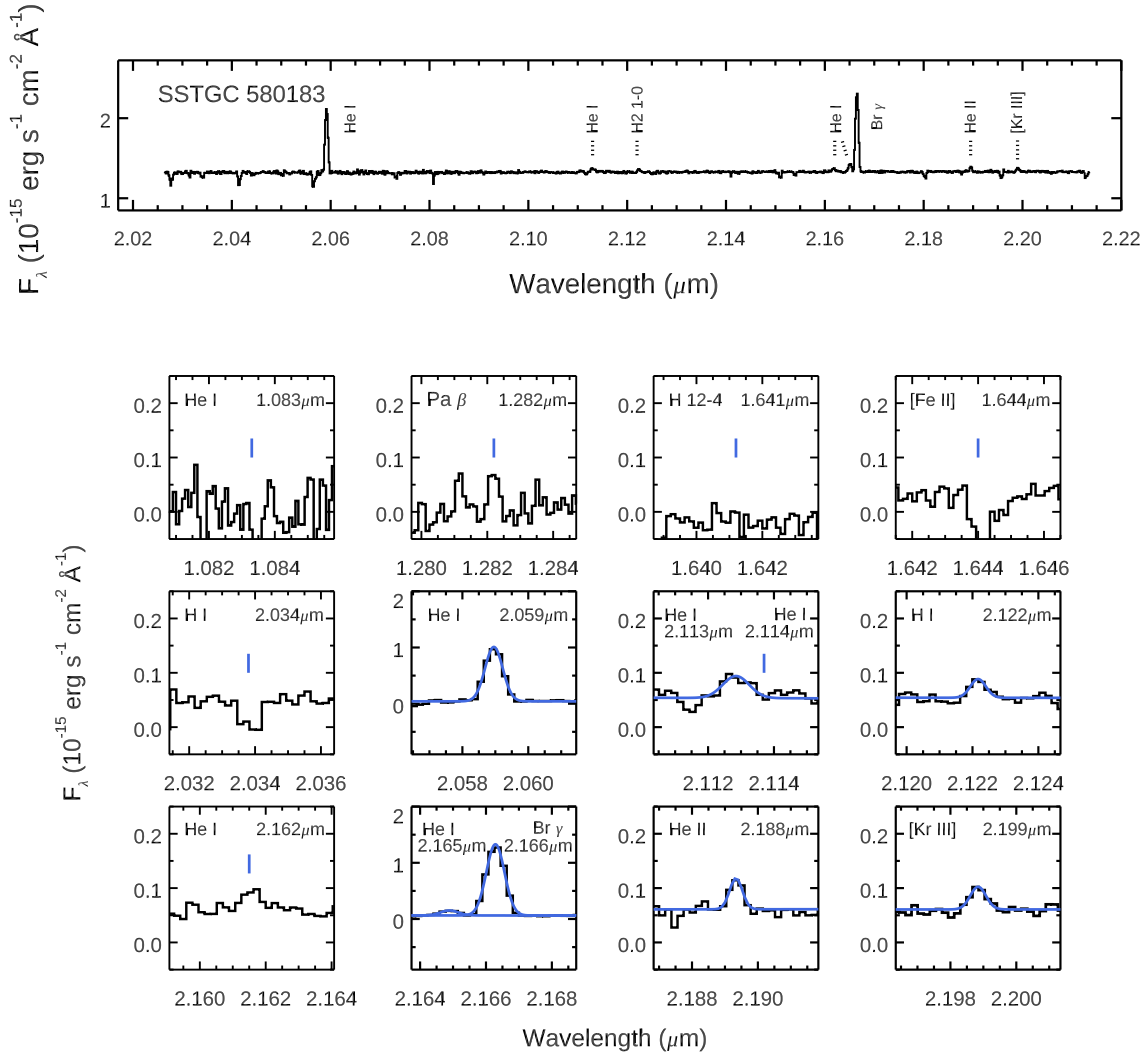


Figure 6. GNIRS spectra of SSTGC 580183. The other spectral orders are omitted, because none of the emission lines are detected at shorter wavelengths.

sian function after subtracting the local continuum using a straight line. For blended lines such as He I ($2.165 \mu\text{m}$) and Br γ , two Gaussians were used to simultaneously fit both emission lines. Flux uncertainties indicate the difference between the best-fitting Gaussian and a direct summation of the continuum-subtracted line fluxes. A 3σ upper limit is shown if the lines are not detected, as is the case for most of the short-wavelength lines in SSTGC 580183. The heliocentric radial velocities (v_r^{helio}) are the flux-weighted, averaged values from the observed lines, and the uncertainties represent the standard deviation of these measurements. Radial velocities with respect to the local standard of rest (LSR) are also given (v_r^{LSR}).

3.2. Foreground Extinction Estimates

As seen from Br γ emission, which is stronger than Pa β , both objects suffer strong attenuation by a large amount of foreground dust in the Galactic disk. Such a high extinction implies a large distance from the Sun, as we discuss below. However, it also means that modeling emission lines is sensitively affected by the adopted foreground extinction. The impacts of extinction corrections on IR lines are not as significant as those required at optical wavelengths, but systematic differences in the IR extinction curves, as demonstrated below, and patchy extinction toward the CMZ generally make extinction corrections difficult.

Table 2 lists individual extinction estimates from the observed Br γ and Pa β lines for each object, based on three near-IR extinction curves (Chiar & Tielens 2006; Boogert et al. 2011; Fritz et al. 2011). For the estimate derived from Chiar & Tielens (2006), we employed their

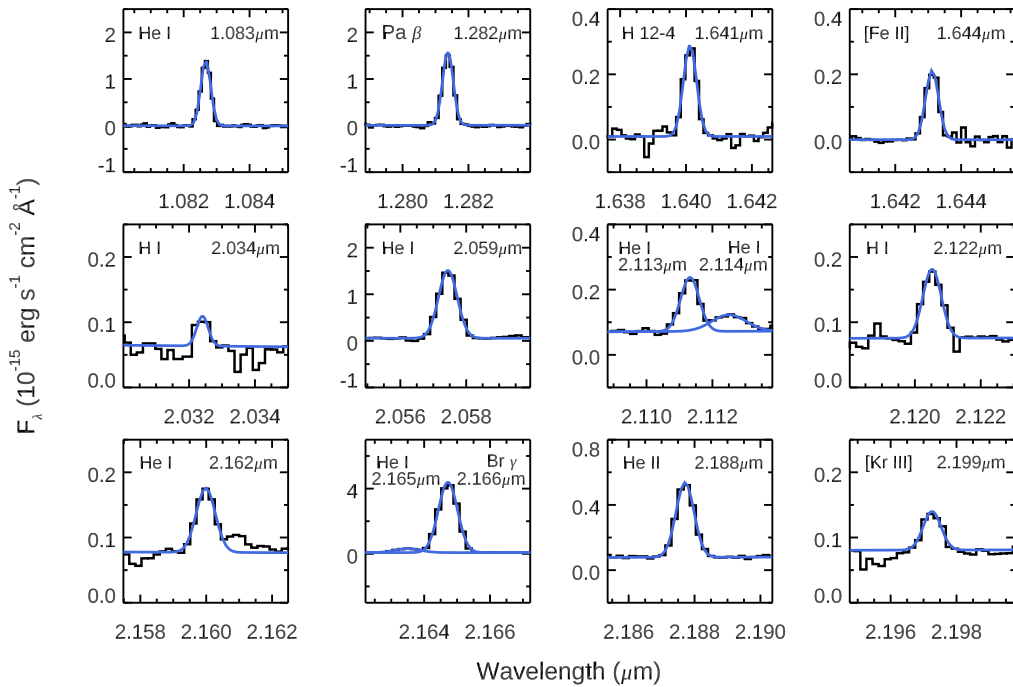
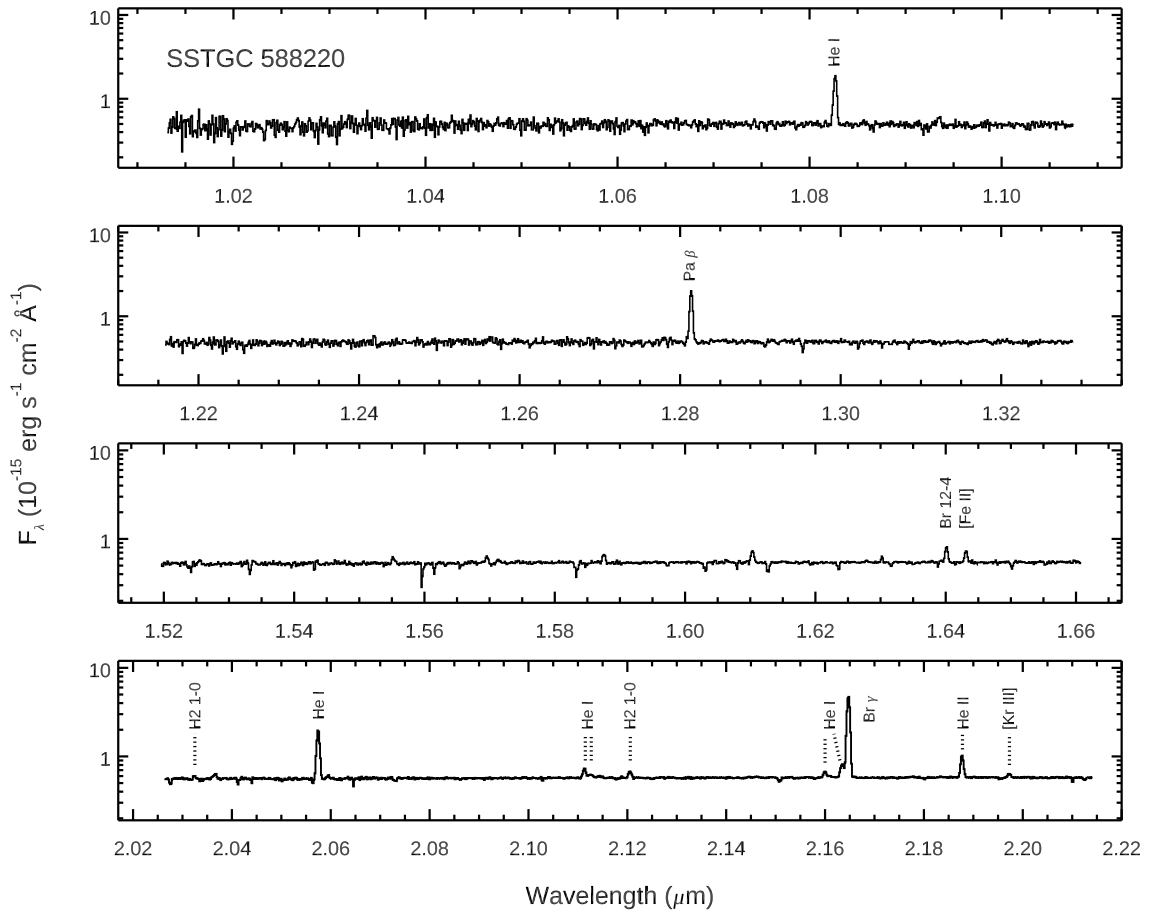


Figure 7. GNIRS spectra of SSTGC 588220.

Table 2. Foreground Extinction Estimates

Extinction	SSTGC 580183 ^a	SSTGC 588220
A_K (Fritz et al. 2011)	> 2.72	1.74 ± 0.03
A_K (Chiar & Tielens 2006)	> 3.64	2.33 ± 0.04
A_K (Boogert et al. 2011)	> 3.95	2.53 ± 0.05
Weighted average $\langle A_K \rangle$	> 3.26	2.09 ± 0.48
Weighted average $\langle A_V \rangle^b$	> 29.7	19.0 ± 4.4
$\langle \tau_{9.6} \rangle^c$	> 5.06	3.24 ± 0.71
$\langle A_K \rangle$ (Schultheis et al. 2009) ^d	3.76 ± 0.49	2.90 ± 0.17
$\langle \tau_{9.6} \rangle$ (An et al. 2013) ^e	2.89 ± 0.37	3.69 ± 0.31
$\langle \tau_{9.6} \rangle$ (Simpson 2018)	2.73	2.80

NOTE—Uncertainties are the 1σ standard deviation of each estimated variable.

^a 3σ upper limits, unless uncertainties are indicated.

^b Assuming $A_K/A_V = 0.11$ (Figer et al. 1999).

^c Assuming $1.3 \leq \tau_{9.6}/A_K \leq 1.8$ (see text).

^d Extinction within $2'$ of the source.

^e Extinction within $0.9'–1.5'$ of the source.

extinction curve in the line of sight to the GC. The 3σ upper limit on Pa β was used to constrain the foreground extinction toward SSTGC 580183. We assumed the Case B emissivity ratios from Storey & Hummer (1995), $j(\text{Pa } \beta)/j(\text{Br } \gamma) = 5.875$, at a typical nebular electron temperature ($T_e = 10^4$ K) and density ($N_e = 10^3 \text{ cm}^{-3}$) (e.g., Zhang et al. 2004) and compared them to the observed line ratios to derive the extinction at $2.2 \mu\text{m}$, A_K . The uncertainties are the quadratic sum of the propagated values from the flux measurement uncertainties and systematic differences from other Case B conditions ($2 \times 10^3 \leq T_e \leq 2 \times 10^4$ K and $10^2 \leq N_e \leq 10^4 \text{ cm}^{-3}$).

As shown in Table 2, all of the three extinction curves produce large A_K for both objects, as expected from the observed Br γ and Pa β line ratios. However, the exact values of the foreground extinction strongly depend on the adopted extinction curve. In particular, the curve of Fritz et al. (2011) has the largest slope in the near-IR among the three curves, which results in a systematically smaller A_K by $\sim 30\%$. The differences among the three extinction laws exceed the observational uncertainties.

Nevertheless, the above extinction estimates for SSTGC 588220 are smaller than the *mean* extinction toward sources in the CMZ. The average foreground extinction toward the CMZ is $\langle A_V \rangle \approx 30$ mag, or $\langle A_K \rangle \approx 3.3$ mag, if $A_K/A_V = 0.11$ is adopted (Figer et al. 1999). The A_K from Fritz et al. (2011) is almost a factor of 2 lower than this average. In the case of SSTGC 580183, where we used a 3σ upper limit on Pa β , the foreground

extinction estimates are slightly larger than the GC average, except from the Fritz et al. curve.

In Table 2, *local* values of the mean foreground extinction are also included. Schultheis et al. (2009) provided an extinction map across the CMZ, based on the IR colors of red giant branch stars in a grid of $2' \times 2'$. The A_K represents the mean and standard deviation of their measurements within $2'$ from each source. Taking $A_K/A_V = 0.11$, their estimates correspond to $A_V \sim 30–40$, which is consistent with the average extinction toward the GC. While the Schultheis et al. (2009) map represented the bulk average of foreground extinction toward each source, An et al. (2013) provided local extinction that is more specific to their lines of sight. In practice, An et al. (2013) followed the procedure in Simpson et al. (2007), and estimated the optical depth at $9.6 \mu\text{m}$ ($\tau_{9.6}$) from the flux ratio between 10 and $14 \mu\text{m}$, measuring the strength of the silicate absorption band centered at $9.6 \mu\text{m}$ (see also Simpson 2018). The $\langle \tau_{9.6} \rangle$ and its uncertainty are the average and standard deviation from four nearby *Spitzer*/IRS slits (within $0.9'–1.5'$ of the sources) that were originally designed to measure background CMZ emissions (An et al. 2009, 2011).

In contrast, Simpson (2018) estimated values of $\tau_{9.6} = 2.725$ for SSTGC 580183 and 2.803 for SSTGC 588220, using a combination of the shapes of the $10 \mu\text{m}$ silicate feature and the [S III] $18.7 \mu\text{m}/33.5 \mu\text{m}$ line ratios. We emphasize that these extinction values, like those from An et al. (2013), apply to the diffuse ISM in the GC and not to objects much smaller than the *Spitzer* IRS apertures that may be substantially in front of (or behind) the CMZ of the GC.

The conversion between A_K and $\tau_{9.6}$ also depends on the shape of the extinction curve over the wavelength interval. If $A_V/\tau_{9.6} = 9$ (Roche & Aitken 1985) is taken, along with $A_K/A_V = 0.11$, $\tau_{9.6}/A_K$ becomes unity. The two extinction curves employed in this work predict $\tau_{9.6}/A_K = 1.3$ (Chiar & Tielens 2006) and 1.8 (Fritz et al. 2011), implying relatively strong silicate absorption with respect to A_K . In Table 2, $\langle \tau_{9.6} \rangle$ is the mean from the two cases with the Chiar & Tielens (2006) and Fritz et al. (2011) laws, while the uncertainty indicates half of the difference. The $\tau_{9.6}$ estimates from the GNIRS spectra are $15\%–20\%$ smaller than the ISM extinction measurements from An et al. (2013), implying that the source is likely located in front of gas and dust in the CMZ. Taking these at face value, the larger A_K from background giants (Schultheis et al. 2009) also implies a shorter distance to SSTGC 588220 than to the GC. In the case of SSTGC 580183, the 3σ upper limits are comparable to the foreground extinction from

Schultheis et al. (2009), while they are higher than the An et al. (2013) estimates.

3.3. Comparison to the Size vs. Surface Brightness Relations of PNe

Galactic and extra-Galactic PNe exhibit a tight correlation between the radius and surface brightness (e.g., Frew et al. 2016b; Stanghellini et al. 2020, see Figures 8 and 9), according to which a smaller PN tends to have a higher mean surface brightness. Because other astrophysical nebulae, such as classical nova shells, show noticeable offsets from this relation (e.g., Frew et al. 2016a), its direct comparison can be used not only to confirm the nature of our sources as PNe, but also to constrain a distance range assuming that our sources directly follow the mean PN relation.

For this comparison, we measured the angular size of SSTGC 588220 from the *HST*/NICMOS Pa α image (Wang et al. 2010). Since the bright inner rim shows a mild ellipticity (Figure 4), we took the average of the angular diameter measured along the major and minor axes, $2.83 \pm 0.02''$. Reassuringly, this size is comparable to the spatial extent of the observed emission line profiles (Figure 5). On the other hand, emission lines from SSTGC 580183 show double peaks along the slit, and the observed full extent is approximately equal to the mean diameter from high-resolution radio images (Zhao et al. 2020), $3.86 \pm 0.04''$.

For our targets, the H α and H β fluxes were computed from the extinction-corrected Br γ line flux, assuming the same Case B recombination coefficients as in the previous section: $j(\text{H}\alpha)/j(\text{Br}\gamma) = 103.0$ and $j(\text{H}\beta)/j(\text{Br}\gamma) = 36.1$ (Storey & Hummer 1995). Over $5 \times 10^3 \leq T_e(K) \leq 2 \times 10^4$ and $10^2 \leq N_e \leq 10^4$, the ranges of these coefficients are 92.2–118 and 30.3–43.0, respectively. Because the GNIRS targets are more extended than the slit width, we estimated the amount of light lost by simulating our observations with the continuum-subtracted *HST* Pa α images (Wang et al. 2010). From this, we found that the $0.675''$ -wide slit collects approximately $41\% \pm 3\%$ of the total light from SSTGC 588220. Similarly, we used the 5.5 GHz map (Zhao et al. 2020) for SSTGC 580183 to compute the surface area covered by the slit, $18\% \pm 4\%$, assuming a 20% uncertainty in this measurement.

To compute uncertainties in the surface brightness estimates, we considered various sources of systematic errors, such as those from the angular diameter measurements, light loss correction, and Case B recombination coefficients, as presented above. In addition, since the H α and H β line fluxes depend on which of the three extinction curves included in this study is taken, we explic-

itly included it as a source of systematic uncertainties. We also assumed a 20% uncertainty in the absolute flux calibration. The final uncertainties were computed by adding in quadrature the above systematic errors and the flux measurement uncertainties.

Figure 8 shows the radius versus H β surface brightness relation of the Galactic PNe in Stanghellini et al. (2020), which is based on accurate distances to the PNe central stars from *Gaia* DR2 (Gaia Collaboration et al. 2018). A comparison to our GNIRS observation for SSTGC 580183 and SSTGC 588220 is shown in the top and bottom panels, assuming that they are located in the GC at a distance of $d_\odot = 8.2$ kpc (Gravity Collaboration et al. 2019; Reid et al. 2019). In both panels, the average H β surface brightness estimated from the GNIRS Br γ flux is shown by blue open diamonds, assuming an average extinction toward each object (Table 2). Since the lower limit on the extinction correction is available for SSTGC 580183, its 3σ lower limit is marked. The vertical error bars indicate the quadrature sum of the uncertainties as described above. The horizontal error bars show an approximate range of the physical radius, assuming that they are located in the Galactic bulge at $d_\odot = 8.2 \pm 2.0$ kpc (see below for independent derivations of the distances).

The gray crosses in Figure 8 indicate the individual Galactic PNe in Stanghellini et al. (2020). There is a significant scatter of points below the relation at smaller radii, which is attributed to the low ionized-masses ($< 0.01 M_\odot$) of these objects among other possible causes (see discussion in Stanghellini et al. 2020). Accordingly, if our candidate PNe do not follow the mean size versus surface brightness relation, but are outliers with systematically smaller radii, the inferred distances would become significantly larger by an order of magnitude. However, the ionized-masses of SSTGC 580183 and SSTGC 588220 based on radio fluxes (~ 0.4 – $3 M_\odot$ assuming 4–8 kpc distances) are larger than the upper limit for their outliers, rejecting hypothesis. The solid line shows the best-fitting relation to the data in Stanghellini et al. (2020) without the low ionized-mass sample.

In addition, Figure 9 shows comparisons to the size versus H α surface brightness relation of the Galactic and extra-Galactic PNe of Frew et al. (2016b). The gray crosses indicate the Galactic and extra-Galactic ‘calibrator’ sample in their study, which do not show the same large scatter at small radii as that in Figure 8. The black solid line indicates their best-fitting relation to all sample PNe. The dotted and dashed lines show the observed relations for bulge and disk PNe in the Milky

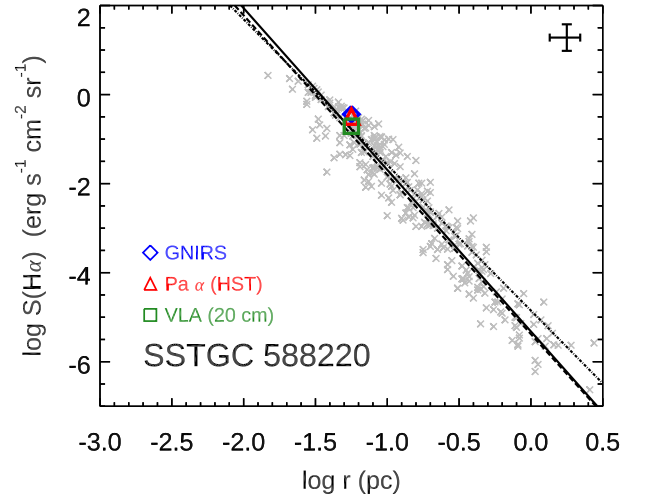
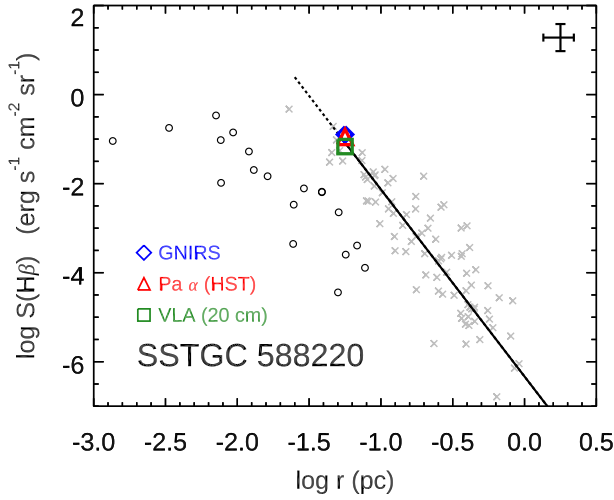
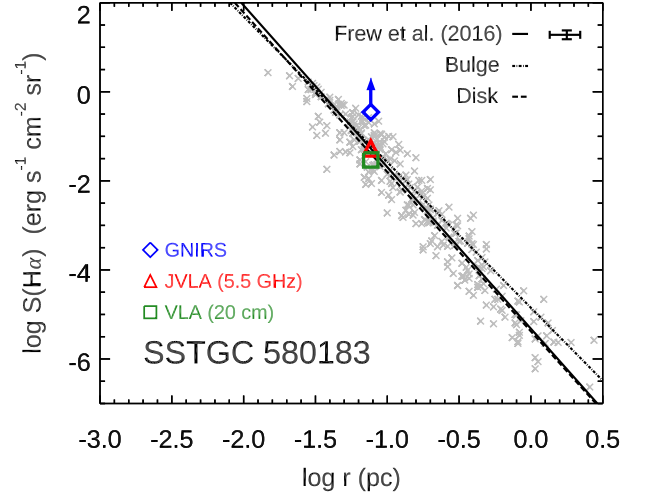
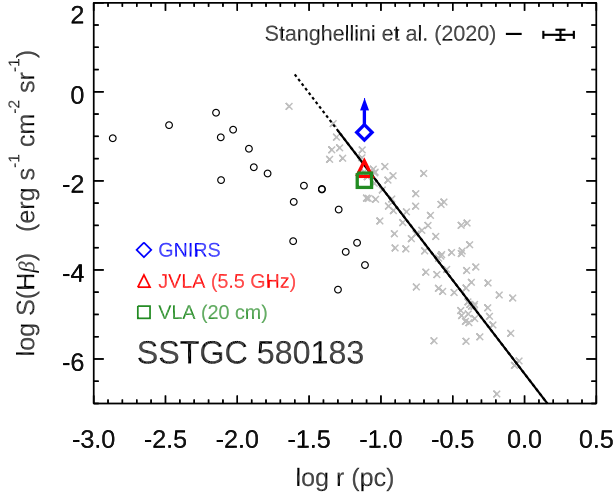


Figure 8. Comparisons of SSTGC 580183 (top) and SSTGC 588220 (bottom) to the radius versus $H\beta$ surface brightness relation of PNe in Stanghellini et al. (2020). The surface brightness estimates from GNIRS observations are indicated by the blue open diamonds. Other measurements from JVLA 5.5 GHz (Zhao et al. 2020, red triangle at the top), VLA 20 cm (Yusef-Zadeh et al. 2004, green boxes), and *HST* Pa α observations (Wang et al. 2010, red triangle at the bottom) are also shown assuming that the sources are located at the GC distance ($d_{\odot} = 8.2$ kpc). For the purpose of comparison, representative error bars are shown for $\Delta d_{\odot} = \pm 2$ kpc (see text). The GNIRS-based estimate for SSTGC 580183 indicates a 3σ lower limit. The gray crosses are Galactic PNe in Stanghellini et al. (2020), and the open circles indicate a subset of these with low ionized-mass (see their Figure 3); their best-fitting power law is shown by a solid line, and its extrapolation beyond the sample limit is indicated by a dotted line.

Figure 9. Same as Figure 8, but showing comparisons to the radius versus $H\alpha$ surface brightness relation in Frew et al. (2016b). The relations derived from Galactic bulge and disk populations are indicated by the dotted and dashed lines, respectively. The best-fitting power law of their full calibrator sample is shown by a solid line.

Way, respectively, which are not significantly different from each other and from the mean relation.

In all cases, the GNIRS observations are in good agreement with the PN relations if the sources are put at the GC distance. The same conclusion can be drawn using the Pa α flux measurement from *HST*/NICMOS for SSTGC 588220 (red open triangles in the bottom panels of Figures 8 and 9). As an independent check on these results, we also employed radio continuum fluxes from VLA 20 cm (Yusef-Zadeh et al. 2004) and JVLA 5.5 GHz observations (Zhao et al. 2020) to infer their $H\alpha$ and $H\beta$ surface brightnesses, which are essentially free

Table 3. Heliocentric Distance Estimates

Observations/Relation ^a	SSTGC 580183 ^b	SSTGC 588220
Br γ /Frew et al.	< 4.8 kpc	6.5 \pm 1.8 kpc
Br γ /Stanghellini et al.	< 5.5 kpc	7.4 \pm 1.5 kpc
Pa α /Frew et al.	...	6.7 \pm 1.8 kpc
Pa α /Stanghellini et al.	...	7.6 \pm 1.5 kpc
20 cm/Frew et al.	9.5 \pm 1.5 kpc	7.7 \pm 1.4 kpc
20 cm/Stanghellini et al.	9.9 \pm 2.1 kpc	8.6 \pm 1.9 kpc
5.5 Ghz/Frew et al.	8.1 \pm 1.3 kpc	...
5.5 Ghz/Stanghellini et al.	8.6 \pm 1.8 kpc	...
Average	9.0 \pm 1.6 kpc ^c	7.6 \pm 1.6 kpc

NOTE—Uncertainties are the 1σ standard deviation of each estimated variable.

^a Observations: Wavelengths at which fluxes were measured to derive surface brightness – Br γ (this study), Pa α (Wang et al. 2010), 20 cm (Yusef-Zadeh et al. 2004), and 5.5 GHz (Zhao et al. 2020). Relations: Surface brightness versus size relations of PNe in Frew et al. (2016b) and Stanghellini et al. (2020) used to compute the physical size of a PN.

^b 3σ upper limits, unless uncertainties are indicated.

^c Weighted average distance from radio observations.

of extinction errors. Moreover, the radio images encompass the whole structure of each target and therefore do not need slit-loss corrections. We employed the relation between the hydrogen recombination line flux and the free-free emission in Scoville et al. (2003) and assumed the same set of recombination line Case B emissivities in the previous section. The surface brightness estimates derived from radio fluxes are marked by green boxes (VLA 20 cm) and red triangles (JVLA 5.5 GHz; top panels) in Figures 8 and 9, which show good agreement with both the Frew et al. (2016b) and Stanghellini et al. (2020) relations.

Assuming that our candidate PNe follow the surface brightness versus radius relations in the above two studies, we proceed to constrain the range of distances to each object by directly comparing its measured angular size to the inferred physical size for the estimated average surface brightness. The heliocentric distances computed in this way are summarized in Table 3. The first two rows show distance estimates using the Br γ fluxes measured with GNIRS in this study, based on Frew et al. (2016b) and Stanghellini et al. (2020), respectively. For SSTGC 580183, upper distance limits are shown from the lower limit in the foreground extinction. The uncertainties include those propagated from the surface brightness measurements and the fitting coefficients in each of the relations. Within the uncertainties, both PN relations give consistent distance estimates with each other for each PN candidate.

Table 4. Physical Parameters Used in the Cloudy Models

	SSTGC 580183	SSTGC 588220
T_{eff} (K) ^a	105,947	131,856
Log $Q(\text{H})$ (s^{-1})	46.892	47.194
Inner Radius (pc)	0.0250	0.02235
Electron Density (N_e ; cm^{-3})	5425 \pm 2300	1580 \pm 800
Hydrogen Density (N_H ; cm^{-3})	3606	3025
Filling Factor (f)	0.1000	0.2861

^a Effective temperature of an ionizing star from stellar atmosphere models at $\log g = 6$ (Rauch 2003).

As shown in Table 3, the distances to SSTGC 588220 derived from the near-IR line fluxes are slightly smaller than those estimated using radio flux measurements, although they are in mutual agreement within the estimated uncertainties. On the other hand, the 3σ upper distance limits for SSTGC 580183 seem too small compared to those derived from radio fluxes. This implies that our estimated foreground extinction toward SSTGC 580183 may be too large, or that there may be systematic errors in the adopted extinction curves. The average distance to SSTGC 580183 in Table 3 indicates a mean distance from radio observations; an average distance to SSTGC 588220 is derived from near-IR and radio observations. These average distances, as well as the high foreground extinction, indicate that both targets are likely located in the central region of the Milky Way.

4. NEBULAR ABUNDANCES

4.1. Cloudy Models

Estimates were made of the abundances of the two candidate PNe using Cloudy 17.02 (Ferland et al. 2017). The input parameters to the Cloudy models are summarized in Table 4. These parameters were estimated by computing a large number of models with varying values of the effective temperature (T_{eff}) of the exciting star (here $\log g = 6$ white dwarf models at solar abundance taken from Rauch 2003), the hydrogen nucleus density N_H (the electron density N_e being variable with depth in the models depending on the local ionization of the multielectron elements), the filling factor f (see Simpson 2018, for equations relating N_H and f), and the abundances of helium and the heavy elements (see below). The total ionizing luminosities $Q(\text{H})$ (number of photons s^{-1}) were estimated from the radio fluxes measured by Zhao et al. (2020) for SSTGC 580183 and by Yusef-Zadeh et al. (2004) for SSTGC 588220, with the assumption of a rounded GC distance of $d_{\odot} = 8$ kpc, $T_e = 10^4$ K, and the use of Equa-

tion (1) of [Simpson & Rubin \(1990\)](#). The inner radii were measured from Figures 3 and 4, and were scaled at $d_{\odot} = 8$ kpc. The final models presented in Tables 5 and 6 were selected as those that best fit the measured, extinction-corrected line flux ratios, with an emphasis on the lines with the highest fractional ionization if multiple ionization states were observed. We note that, since all model comparisons are made using line flux ratios, the results for the abundances estimated from the models will not change if the estimated distances are slightly different from $d_{\odot} = 8$ kpc.

In this modeling effort, we included various mid-IR lines measured with *Spitzer* IRS, in addition to the hydrogen and helium lines observed with GNIRS. We utilized the line intensity measurements from [Simpson \(2018\)](#), which were based on the spectral extraction tool CUBISM ([Smith et al. 2007](#)) with point-source flux calibration. All of the lines were measured by fitting Gaussians to the spectra. Some lines were remeasured in this study using the IRS analysis program SMART-IDEA ([Higdon et al. 2004](#)) for better accuracy. These include [S IV] 10.51, [Ar V] 13.10, [Mg V] 13.52, [Fe VI] 14.77, [P III] 17.88, [Fe II] 17.94, [Ar III] 21.83, [Ne V] 24.32, and [Fe III] 22.93 μm . As described in § 2, background subtraction was performed on a line-by-line basis by taking the average of the high-resolution (IRS SH and LH modules) fluxes at four nearby positions, while for the low-resolution modules (SL and LL), background positions were measured from slightly distant positions along the same slits.

In Table 5, the extinction-corrected line fluxes are expressed as line ratios with respect to the hydrogen recombination lines, where H I 7–4 (Br γ) was used for those observed with GNIRS, and H I 7–6 (12.37 μm) for the IRS observations. The division into two wavelength intervals was necessary to minimize systematic errors from the different slit sizes – the GNIRS observations were made with a relatively narrow slit (slit models), while the longer-wavelength IRS slits were large enough (minimum slit width 3.6'') to include the whole source (whole nebula models). We corrected the observed near-IR line fluxes for extinction using A_K estimates derived from the [Fritz et al. \(2011\)](#) extinction curve (Table 2). The same extinction curve was used for the mid-IR emission lines up to the peak of the 9.7 μm silicate feature. At longer wavelengths, however, we employed the [Chiar & Tielens \(2006\)](#) extinction curve because it extends to a longer wavelength (~ 35 μm instead of the 27 μm of [Fritz et al. 2011](#)). Also, it is based on a source that should have absorption only (the Quintuplet cluster star GCS 3) and not on a source for which one must compensate for dust emission (Sgr A) in the extinction

curve estimate at the longest wavelengths ([Fritz et al. 2011](#)). The uncertainties in the background-subtracted line intensities include uncertainties from the flux measurements and the background subtraction, which are added in quadrature.

For the reasons described above, we performed separate Cloudy runs to account for the slit models and the whole-nebula models. In the former, computed by integrating the line volume emissivities over a simulated long slit, the near-IR lines Br γ , He I 2.059 μm , and He II 2.189 μm lines were used to produce estimates of T_{eff} and the He/H ratio.⁴ In the whole-nebula models, the mid-IR lines, computed by integrating over the whole volume, were used to produce estimates of N_{H} , the abundances of the heavy elements, and f for SSTGC 588220. Aside from these details of the integration, all the model parameters (density, temperature, abundances, etc.) were identical for both slit and whole-nebula models. The real objects, of course, do not have constant density, but we do not have enough data to attempt to model the effects of density variations.

We used Cloudy with its ‘optimize’ commands, whereby, in each call, a given parameter or set of parameters is allowed to vary with the best solution based on the deviation of the model predictions for a set of lines with the observed fluxes. Because of the large number of input parameters, relative to the limited observational information, a uniform density and a constant filling factor were assumed in these models. The elemental abundances were fit by hand by comparing the model output with the observed line flux ratios. The filling factor was computed by optimize command for SSTGC 588220, but this was not successful for SSTGC 580183. Instead, models with a variety of filling factors were computed and the median model with $f = 0.10$ was selected.

Elemental abundances in the models, other than those derived in the modeling, were taken from Cloudy’s standard set for PNe, which we revised to use the more recent observations of C/O and N/O ratios of [Stanghellini & Haywood \(2018\)](#). Whereas the Cloudy standard PN abundances are greatly enriched in carbon (C/O > 1), when we computed the medians of [Stanghellini & Haywood \(2018\)](#) tabulated logarithmic carbon, nitrogen, and oxygen abundance differences, we found ratios C/O = 0.767 and N/O = 0.372. The latter ratio is close to the Cloudy standard PN abundance ratio and is substantially higher than typical H II region abun-

⁴ The other K -band He I lines are listed here by their most important components, but are actually blends with lines that are distinguished in Cloudy. We are unable to separate them owing to the moderate spectral resolution of our data.

Table 5. Normalized Line Fluxes

Emission Line	Wavelength (μm)	SSTGC 580183				SSTGC 588220			
		Observation		Model		Observation		Model	
		Flux ^a	Uncertainty ^b	Flux ^c	Ion. ^d	Flux ^a	Uncertainty ^b	Flux ^c	Ion. ^d
<i>Gemini GNIRS (slit models)</i>									
Pa β	1.2822	5.877	0.015	5.579	-0.028
Br 12-4	1.6412	0.168	0.031	0.186	-0.028
Br γ	2.1661	1.000	0.047	1.000	-0.037	1.000	0.014	1.000	-0.028
He I 2^3P-2^3S	1.0833	40.445	0.020	8.412	-0.221
He I 2^1P-2^1S	2.0587	0.9846	0.079	0.9840	-0.046	0.4003	0.015	0.4001	-0.221
He I 4^3P-3^3S	2.1128	0.0532	0.070	0.0388	-0.046	0.041	0.046	0.016	-0.221
He I 4^1P-3^1S	2.1137	0.023	0.336	0.006	-0.221
He I 7^3F-4^3F	2.1615	0.023	0.070	0.011	-0.221
He I 7^3G-4^3F	2.1649	0.075	0.087	0.017	-0.221
He II 10-7	2.1884	0.0285	0.101	0.0285	-1.256	0.0966	0.020	0.0968	-0.426
[Fe II]	1.6440	0.225	0.203	11.93	-0.825
[Kr III]	2.1990	0.02745	0.437	...	-0.437	0.0122	0.0929	...	-0.534
<i>Spitzer IRS (whole nebula models)</i>									
H 7-6	12.3719	1.000	0.055	1.000	-0.052	1.000	0.099	1.000	-0.041
[O IV]	25.8903	63.7	0.15	63.85	-1.931	330.95	0.102	330.98	-0.869
[Ne II]	12.8135	41.8	0.057	49.17	-0.765	15.57	0.111	29.94	-1.193
[Ne III]	15.5551	408.6	0.056	346.4	-0.092	413.37	0.099	477.8	-0.110
[Ne V]	14.3217	-5.209	160.13	0.099	137.5	-1.669
[Ne V]	24.3175	-5.209	113.35	0.099	94.0	-1.669
[Na III]	7.3169	5.36	0.077	5.34	-0.158	-0.156
[Mg V]	13.5213	-5.966	0.654	0.283	0.652	-1.772
[P III]	17.8850	0.92	0.47	0.914	-0.448	1.716	0.307	1.716	-0.411
[S III]	18.7130	120.3	0.057	106.64	-0.256	81.82	0.102	92.22	-0.295
[S III]	33.4810	36.7	0.23	32.55	-0.256	40.02	0.316	34.53	-0.295
[S IV]	10.5105	93.4	0.056	105.27	-1.052	245.80	0.099	218.1	-0.670
[Cl II]	14.3678	1.25	0.067	1.246	-0.535	-0.750
[Ar II]	6.9853	14.5	0.088	9.81	-1.091	-1.309
[Ar III]	8.9910	35.6	0.068	86.73	-0.089	-0.172
[Ar III]	21.8302	5.82	0.121	5.19	-0.089	4.626	0.121	4.62	-0.172
[Ar V]	13.1022	-2.796	6.031	0.101	20.38	-1.276
[Fe III]	22.9250	4.35	0.145	4.34	-0.587	17.67	0.110	17.63	-0.669
[Fe VI]	14.7710	-3.199	0.446	0.139	14.32	-1.207

^a Extinction-corrected observed line fluxes with respect to Br γ (GNIRS) from Table 1 or H I 7-6 12.37 μm (IRS, [Simpson 2018](#)).

^b Uncertainties in the observed line flux ratios, consisting of the statistical uncertainties from the line flux measurements combined quadratically with the uncertainty of the associated hydrogen recombination line.

^c Modeled line fluxes with respect to Br γ or H I 7-6 12.37 μm .

^d Logarithm of the fractional ionization of each ion.

dance ratios (e.g., [Simpson 2018](#)). For silicon, we used the GC Si/O ratio of 0.035 from [Simpson \(2018\)](#). As we varied the oxygen abundance in the models, we also varied the C, N, and Si abundances in accordance with these ratios. Since we observed neon and argon lines directly, we did not need to use the [Stanghellini & Haywood \(2018\)](#) ratios. The graphite and silicate grain opacities were included in the calculation.

The criteria for an acceptable fit and the steps in the modeling process were as follows:

(i) The He II 2.189 μm /He I 2.059 μm line ratio, which was used to estimate the T_{eff} of the PN central star, should be equal to the observed ratio. Iteration was needed, since the exact T_{eff} is somewhat dependent on N_{H} and f as they both affect the ionization parameter U ([Simpson 2018](#), their Equation 2).

(ii) Density-sensitive line pairs (mainly [S III] 18.7 μm and 33.5 μm , but also [Ne V] 14.3 μm and 24.3 μm for SSTGC 588220) should agree with the observed line ratios; the [Ar III] 8.99 μm and 21.8 μm line pair in SSTGC 580183 was not used because of the large uncer-

Table 6. Elemental Abundances

Elements	SSTGC 580183	SSTGC 588220	Solar ^b
Hydrogen	12.00	12.00	12.00
Helium	11.16 ± 0.04	10.86 ± 0.03	[10.93]
Oxygen	9.52 ± 1.85	8.95 ± 0.35	8.69
Neon	8.64 ± 0.04	8.67 ± 0.04	[7.93]
Sodium	6.84 ± 0.06	...	6.21
Magnesium	...	8.05 ± 1.29	7.60
Phosphorus	5.78 ± 0.16	5.86 ± 0.16	5.41
Sulfur	7.59 ± 0.18	7.36 ± 0.22	7.12
Chlorine	5.75 ± 0.10	...	5.50
Argon	7.13 ± 0.04	6.99 ± 0.08	[6.40]
Iron	6.99 ± 0.19	7.53 ± 0.15	7.47
Krypton ^c	4.16 ± 0.20	3.67 ± 0.06	[3.25]

^a Solar abundances from [Asplund et al. \(2009\)](#) with the exception of Na, Mg, and Fe, which are from [Scott et al. \(2015a,b\)](#). The brackets around the noble gas abundances indicate that these solar abundances are ‘indirect photo-spheric estimates’ ([Asplund et al. 2009](#)).

^b Krypton was modeled separately from the Cloudy runs (see text).

tainties. As shown in the high-resolution images (bottom panel of Figures 3 and 4), the PNe may not have a constant density. Indeed, it was not possible to find constant-density models that produced line ratios that agreed with all line pairs. For this reason, less weight was given to the [S III] line pair in SSTGC 588220, which has larger uncertainties than the [Ne V] line pair.

(iii) The line ratios with respect to hydrogen should agree with the observed ratios. To ensure this, the relative abundances of helium and the heavy elements were adjusted in each iteration. In the models, the abundances of carbon, nitrogen, and silicon, all unobserved in our candidate PNe, were scaled to the abundance of oxygen as discussed above. This resulted in additional iterations as changing the abundances modifies the cooling function and hence the electron temperature, which in turn affects all computed fluxes and flux ratios.

4.2. Results

The elemental abundances in the best-fitting Cloudy models are given in Table 6. Although we ran models assuming constant N_{H} and f , the above modeling exercise provides useful and reliable information on the central star T_{eff} and, in particular, on the abundances of helium, neon, and sulfur, all of which were observed in lines from more than one ionization stage. Of lesser reliability are the elements observed from only a single ionization stage, although some have, at least, the dominant ionization stage observed. The reliability can be estimated from the sizes of the errors.

Uncertainties in the background subtraction propagate into significant uncertainties in the final abundances for most heavy elements. This is because abundances are tabulated with respect to hydrogen, where the strongest hydrogen line in the IRS wavelength is the H 7–6 line at 12.37 μm , which is sensitive to background subtraction. Whereas the highest-excitation lines have little or no presence in the background spectra, the low-excitation lines have substantial background emission that needs to be removed. In particular, background subtraction removes 27% of the measured target flux of the H 7–6 line for SSTGC 580183, and 40% of the measured target flux for SSTGC 588220 (see Figure 2); the final S/N are 18 and 10 for SSTGC 580183 and SSTGC 588220, respectively (Table 5). The other singly ionized lines ([Ne II], [Ar II], and [Fe II]) have even more flux subtracted (so much so for [Fe II] that this line was dropped from the analysis), but these elements have doubly ionized lines in the IRS spectra, which make our abundance estimates more secure. For these calculations, the measurement uncertainty includes the uncertainty in the background subtraction, computed as the sum, in quadrature, of the measured uncertainties in the line fluxes for target and background positions. It does not include any calibration uncertainty or estimation of any nonlinear departures from a smoothly sloping background.

The abundance uncertainties in Table 6 are the sum, in quadrature, of the measurement uncertainty, the uncertainty due to a possible error in the extinction of $\Delta\tau_{9.6} = 0.5$, and an estimate of the model error expressed as the uncertainty in the ionization correction factor (*ICF*). An *ICF* is defined here as the ratio of the total abundance of an element to the abundance of the observed ionization stage as computed by the model. The *ICF* uncertainty is estimated to be the value of 0.05 divided by the fractional ionization of the observed ion for elements where only one ionization state was observed or it is estimated to equal 0.25 times the fractional ionization of the unobserved ionization states when multiple ionization states were observed. Which of these errors dominates depends on the line: the measurement error is important for the two blended lines, [P III] 17.88 μm and [Fe II] 17.94 μm (the latter having such a large uncertainty that it was not further included); the extinction error is mainly important for the lines with wavelengths near 10 μm and 18 μm (this uncertainty is large because the silicate extinction curve is not that well known); and the *ICF* error dominates for lines arising from ions with very low fractional ionization, such as O^{3+} and Mg^{4+} . Finally, the uncertainty for O/H in SSTGC 588220 was increased because the line

was saturated in the high-resolution IRS module (LH) and the flux had to be taken from the low-resolution (LL1) observation.

4.2.1. *SSTGC 588220 (G0.0967-0.0511)*

The fluxes predicted by the Cloudy models provide reasonably good agreement with the observed fluxes. However, in spite of the overall agreement, notable discrepancies are found in some lines. For instance, the best-fitting model overpredicts the fluxes from [Ar V] 13.1 μm and [Fe VI] 14.7 μm , while it underestimated the He I 1.083 μm flux. The overestimated high-excitation lines are probably a result of the source not being spherically symmetric and having large density fluctuations. On the other hand, the He I 1.083 μm line is more sensitive to the amount of extinction than the longer-wavelength He lines, and its emissivity is more dependent on the details of the electron density distribution than the emissivity of the He I 2.059 μm line (see Porter et al. 2012, 2013).

4.2.2. *SSTGC 580183 (G359.9627-0.1202)*

The agreement with the best-fitting model is less satisfactory in the case of SSTGC 580183, most likely due to the PN having components of multiple densities and filling factors, rather than having constant values as assumed in the current analysis. In particular, the optimize command in Cloudy initially produced a very low filling factor ($f \approx 0.03$) in the models, driven by the absence of high-ionization lines such as [Ne V], [Ar V], and [Mg V] in the *Spitzer* mid-IR spectra, except [O IV] 26 μm . The models described in Tables 4 and 5 were produced with $f = 0.1$ (the model parameters do not change appreciably with changing f) and an inner radius of 0.025 pc (estimated from the ring size in Figure 3, bottom). The uncertainties in these tables do not include any uncertainty for choice of model, but an additional $\sim 10\%$ should be added to the abundance uncertainties in the tables to account for variations in the possible model parameters.

Notably, the oxygen abundance from the best-fitting model is supersolar (Table 6). With a low f , the fraction of elements in the highest-ionization states (like O^{3+}) is very small, and the oxygen abundance (O/H) becomes substantially higher than solar. We also searched for models of more compact PNe with lower f and smaller inner radii that produce a higher ionization fraction of oxygen. However, we found that none of these models could produce as strong [O IV] emission as is observed unless the total oxygen abundance is substantially higher than solar. In addition, because the T_{eff} of the central star can be reliably determined from the He II 2.189 μm /He I 2.059 μm line ratio, and both He^{++}

and O^{3+} require > 54 eV photon energies for ionization to that level, the higher oxygen abundance is less affected by the choice of spectral energy distribution of the exciting star.

Along with oxygen, the helium abundance is also significantly higher than in SSTGC 588220. Because the emission from heavy element ions, especially oxygen, is the primary coolant for the gas, increasing their abundances results in lower electron temperatures. The lower temperatures, in turn, increase the emissivities of the hydrogen recombination lines much more than they change the emissivities of the He I 2.059 μm line (see Storey & Hummer 1995; Porter et al. 2012, 2013). The consequence is that the abundance of helium with respect to hydrogen must be increased above solar to match the observed line fluxes.

4.3. *[Kr III] 2.199 μm*

In both candidate PNe, we detected the *s*-process noble gas krypton (Kr) at 2.199 μm , which was first identified in PNe by Dinerstein (2001). From the line flux measurements, we computed $\text{Kr}^{++}/\text{H}^+$ ratios of $(3.98 \pm 1.80) \times 10^{-9}$ and $(1.36 \pm 0.13) \times 10^{-9}$ for SSTGC 580183 and SSTGC 588220, respectively, based on the Br γ emissivities of Storey & Hummer (1995), the effective collisional strengths for Kr^{++} of Schöning (1997), and the transition probabilities for Kr^{++} of Eser & Özdemir (2019). Because [Kr III] 2.199 μm is not modeled in the current version of Cloudy, we adopted the analytical relation for the *ICF* from Sterling et al. (2015) between the Kr^{++}/Kr and S^{++}/S ratios, which show the tightest fit among other ionic ratios (such as Ar^{++}/Ar). In addition, our S^{++}/S ratio is more reliable than Ar^{++}/Ar , because the S^{++} and S^{3+} measurements were made using higher-resolution modules in IRS with less extinction. The Kr/H abundance ratios are included in Table 6. The uncertainties do not include the uncertainty in the *ICF*.

4.4. *Significance*

Krypton is significantly enriched in both of our targets ($[\text{Kr}/\text{Fe}] = 1.4 \pm 0.3$ and 0.4 ± 0.2 for SSTGC 580183 and SSTGC 588220, respectively)⁵, indicating that this *s*-process element has been overproduced, possibly during the late asymptotic giant branch (AGB) evolution. This is in agreement with other lines of evidence supporting their status as PNe (morphology, high-excitation lines,

⁵ Here, we used conventional notation, $[\text{X}/\text{Y}] \equiv \log(N_{\text{X}}/N_{\text{Y}})_{*} - \log(N_{\text{X}}/N_{\text{Y}})_{\odot}$, where $\log N$ indicates the abundances of specific elements.

and a match to the PN size-surface brightness relations) presented in this paper.

The abundance patterns of our targets are generally consistent with those in the GC region. Stars in this region have a bimodal metallicity distribution with peaks at $[\text{Fe}/\text{H}] \sim -0.5$ and $\sim +0.3$, and exhibit an elevated α -element abundance in the metal-poor component, while the metal-rich counterpart shows near-solar abundance patterns (e.g., [Schultheis et al. 2020](#)). Reassuringly, our derived metallicities, $[\text{Fe}/\text{H}] \approx -0.5 \pm 0.2$ for SSTGC 580183 and $[\text{Fe}/\text{H}] \approx +0.1 \pm 0.2$ for SSTGC 588220, coincide with these metallicity peaks. Regarding α -element abundances, SSTGC 588220 shows abundance patterns ($[\text{O}/\text{Fe}] = 0.2$, $[\text{Mg}/\text{Fe}] = 0.4$) that are similar to the mean trend of the APOGEE GC sample ([Schultheis et al. 2020](#)) within $\Delta[\alpha/\text{Fe}] \lesssim 0.1$ dex. On the other hand, the oxygen abundance of SSTGC 580183 is quite uncertain, although the large sulfur abundance ($[\text{S}/\text{Fe}] = 1.0 \pm 0.3$) seems to suggest enhanced light element abundances of this candidate PN.

Our radial velocity measurements are weighted mean values from all observed near-IR lines.⁶ A high positive radial velocity of SSTGC 580183 ($v_r^{\text{LSR}} \sim +70 \text{ km s}^{-1}$) in the fourth Galactic quadrant and an extreme negative radial velocity of SSTGC 588220 ($v_r^{\text{LSR}} = -150 \text{ km s}^{-1}$) in the first quadrant are at odds with the sense of rotation of the nuclear stellar disk (a positive correlation between v_r and l), but there is a large scatter in the v_r vs. l diagram of stars in the nuclear bulge ([Schönrich et al. 2015](#); [Schultheis et al. 2020](#)).

SSTGC 580183 is helium-rich ($N(\text{He})/N(\text{H}) = 0.12$), while SSTGC 588220 has a nearly solar helium abundance. According to the PN classification scheme in [Peimbert \(1978\)](#), the helium abundance of SSTGC 580183 is at the border between helium- and nitrogen-rich PNe (Type I) and other types with normal helium abundances. Since Type I PNe are considered descendants of a massive progenitor star ($> 2 M_\odot$) by their super-helium and super-nitrogen abundances (see also [Stanghellini & Haywood 2010](#)), it is conceivable that the progenitor of SSTGC 580183 is likely to be as massive as $\sim 2 M_\odot$. Such massive stars are not currently present in old stellar populations of the GC, and therefore other formation channels such as binary interactions (e.g., [Minniti et al. 2019](#)) may be a viable path

to the object’s formation. Conversely, SSTGC 580183 may simply be a product of recent star formation in the CMZ ([An et al. 2011](#); [Longmore et al. 2013](#)). Below, we further discuss the possible formation mechanisms of these candidate PNe on the basis of the low detection rate of PNe in the CMZ.

5. DISCUSSION AND SUMMARY

In this paper, we have presented medium-resolution near-IR spectra taken with Gemini/GNIRS of two candidate PNe that were serendipitously found in *Spitzer*/IRS spectra in close lines of sight to Sgr A*. Besides showing strong emission lines in the mid-IR from several high-excitation ions, their appearance in high-resolution images supports their status as PNe. Moreover, our Gemini/GNIRS near-IR spectra reveal strong emission from doubly ionized krypton in both targets, indicating overproduction of s -process elements in the PN envelope. Their membership in the nuclear stellar disk seems feasible from the proximity to the GC on the sky and distances based on a comparison to PN size-surface brightness relations, and is favored by our joint analysis of near- and mid-IR spectra, over membership in other Galactic structural components. Our Cloudy modeling assumes uniform densities and filling factors of these targets, but future observations with high spatial resolution mapping in various near- and mid-IR lines can potentially reveal high-density or even high-excitation structures within the overall morphology of these sources.

The expected number of PNe in the nuclear bulge may be estimated from a comparison with other Galactic stellar components. The total stellar mass of the nuclear bulge ($\sim 1.4 \times 10^9 M_\odot$; [Launhardt et al. 2002](#)) is approximately 10 times smaller than that of the classical bulge. If we assume that most stars in the nuclear bulge are as old as those in the classical bulge ($\gtrsim 10 \text{ Gyr}$), and simply scale the result obtained from the population synthesis models in [Moe & De Marco \(2006\)](#) by stellar mass, there should be a significant number of PNe ($\sim 10^3$) in this region, although this estimate is uncertain by a factor of two or more.

At the other extreme, a strict lower limit on the expected number of PNe may be estimated from a direct comparison with the number of PNe in the Galactic halo, even though the chemical properties and ages of stars in the nuclear disk are significantly different from those in the halo, and may affect the production rate of PNe. On the theoretical side, if we simply scale the expected number for the stellar halo in [Moe & De Marco \(2006\)](#) by mass, the expected number of PNe becomes ~ 50 , but this estimate is quite uncertain. The large

⁶ More precisely, our radial velocity measurements are based on nebular emission lines, and therefore may not be the same as those of the central star of a PN (e.g., [Lorenzo et al. 2021](#)). Since the expansion speed of typical PNe is in the order of a few tens of kilometers per second, our reported values can differ from the radial velocity of a central star by this amount.

reduction in the expected number of PNe is due to the older ages of the stellar halo (a relatively shorter dissipation timescale of stellar envelopes) compared to those of the bulge populations in their models. On observational grounds, there are eight PNe known in the Galactic globular clusters (Jacoby et al. 1997; Minniti et al. 2019). Therefore, one can naively expect $\sim 10^3$ PNe, since the nuclear bulge is ~ 100 times more massive than the entire globular cluster system in the Milky Way. In this regard, the observed paucity of PNe in the nuclear disk raises a more severe problem than that in other Galactic components with predominantly old stellar populations.

To explain the observed scarcity of PNe in the nuclear bulge, the following scenarios can be speculated. Firstly, this may be due to extreme foreground extinction toward the GC. The average extinction toward the CMZ is $A_V \sim 30$ mag, but the patchy extinction can be as high as $A_V > 60$ mag (Schultheis et al. 2009). However, the two PN candidates presented in this work have foreground extinctions that are not exceptionally smaller than those in other fields. Unless PNe in the nuclear disk are preferentially enshrouded by dusty clouds, the large extinction may not be a dominant factor for the low detection rate of PNe. Indeed, extended sources with PN-like morphologies are rare in essentially extinction-free, 20 cm radio continuum images (Yusef-Zadeh et al. 2004), which cover the entire CMZ. Such objects are also unusual in the *HST*/NICMOS Pa α images (Wang et al. 2010), except SSTGC 588220, in spite of a large sky coverage of the survey – a central $\sim 39 \times 15$ arcmin² region of the CMZ, including Sgr A*.

Second, there may exist an observational bias against PNe with large envelope sizes. The two PNe presented in this paper have the most compact sizes (implying early stages of PN evolution) as can be seen from the size-surface brightness distributions of other Galactic and extra-Galactic PNe (see Figures 8 and 9). Their compactness has even made them appear as pointlike sources in the original *Spitzer*/IRAC catalog (Ramírez et al. 2008). As a consequence, there could be more PNe in lines of sight toward the CMZ that are more difficult to detect due to extended envelopes with lower surface brightness in the high source density, highly dust-obscured region.

Third, if the observed lack of PNe in the GC have astrophysical origins, this may indicate that the PN formation channel such as binary interactions (e.g., Minniti et al. 2019) is overpowered by suppression mechanisms that can reduce the envelope mass of AGB stars. Some stars can also skip the AGB phase and directly evolve into hot subdwarfs, if the envelope mass is not high enough. These AGB manqué stars can

be formed from helium-rich progenitor stars by enhanced mass loss during the red giant branch evolution (Bressan et al. 2012). Such helium-rich stars are expected to be more common in a deep potential well, such as in the GC, where chemical enrichment runs relatively fast.

Lastly, while PNe are strikingly rare in the nuclear bulge, the number of observed PNe is not greatly different from what one would expect from ongoing star formation in the CMZ, with a rate of $\sim 0.1 M_\odot \text{ yr}^{-1}$ (e.g., An et al. 2011; Longmore et al. 2013). Since the PN lifetime is approximately $\Delta t \sim 10^4$ years, the total mass of stars formed at any time interval Δt is $\sim 10^3 M_\odot$, if the star formation has proceeded constantly over the past few billion years. If stars as massive as $2 M_\odot$ can evolve into a PN, for the reasons described above, the total mass of PN progenitors would be $\sim 20 M_\odot$ at any time assuming a standard mass function ($\propto M^{-2.3}$). Therefore, the expected number of PNe would become ~ 5 – 10 , if the average progenitor mass is 2 – $4 M_\odot$ in the nuclear bulge. This number is significantly smaller than the above estimates based on Moe & De Marco (2006), which assume that stellar populations in the nuclear bulge are composed entirely of passively evolving old stars. Interestingly, Simpson (2018) found half a dozen more candidates with exceptionally highly-excited lines from neon and/or oxygen, in addition to the two sources included in this study, which serve as good PN candidates in this region. Future high-resolution narrowband imaging or mid-IR spectroscopic surveys will help us hunt for additional PNe in the nuclear bulge.

ACKNOWLEDGMENTS

We thank the anonymous referee for detailed comments, which helped to improve the content and presentation of the paper. We thank Kris Sellgren and Harriet Dinerstein for many helpful and interesting discussions over the years. We thank Thomas Geballe for his technical assistance before and during the observing runs. J.H. and D.A. acknowledge support provided by the National Research Foundation of Korea (NRF) grants funded by the Korean government (MSIT) (No. 2017R1A5A1070354, 2018R1D1A1A02085433, 2021R1A1C1004117).

The Gemini data (Gemini program GN-2016A-Q-42, NOAO prop. ID 2016A-0431), acquired through the Gemini Observatory Archive at the NSF’s NOIRLab and processed using the Gemini IRAF package, are based on observations obtained at the international Gemini Observatory, a program of NSF’s NOIRLab, which is managed by the Association of Universities

for Research in Astronomy under a cooperative agreement with the National Science Foundation on behalf of the Gemini Observatory Partnership: the National Science Foundation (United States), the National Research Council (Canada), Agencia Nacional de Investigación y Desarrollo (Chile), Ministerio de Ciencia, Tecnología e Innovación (Argentina), Ministério da Ciência, Tecnologia, Inovações e Comunicações (Brazil), and Ko-

rea Astronomy and Space Science Institute (Republic of Korea). This work was made possible by observations made from the Gemini North telescope, located within the Maunakea Science Reserve and adjacent to the summit of Maunakea. We are grateful for the privilege of observing the universe from a place that is unique in both its astronomical quality and its cultural significance.

REFERENCES

- Akashi, M., Bear, E., Soker, N., et al. 2018, *MNRAS*, 475, 4794. doi:10.1093/mnras/sty029
- An, D., Ramírez, S. V., Sellgren, K., et al. 2009, *ApJL*, 702, L128. doi:10.1088/0004-637X/702/2/L128
- An, D., Ramírez, S. V., Sellgren, K., et al. 2011, *ApJ*, 736, 133. doi:10.1088/0004-637X/736/2/133
- An, D., Ramírez, S. V., & Sellgren, K. 2013, *ApJS*, 206, 20. doi:10.1088/0067-0049/206/2/20
- Asplund, M., Grevesse N., Sauval A. J., & Scott P. 2009, *ARA&A*, 47, 481. doi:10.1146/annurev.astro.46.060407.145222
- Balick, B. & Frank, A. 2002, *ARA&A*, 40, 439. doi:10.1146/annurev.astro.40.060401.093849
- Beaulieu S. F., Freeman, K. C., Kalnajs, A. J., Saha, P., & Zhao, H. 2000, *AJ*, 120, 855. doi:10.1086/301504
- Boogert, A. C. A., Huard, T. L., Cook, A. M., et al. 2011, *ApJ*, 729, 92. doi:10.1088/0004-637X/729/2/92
- Bressan, A., Marigo, P., Girardi, L., et al. 2012, *MNRAS*, 427, 127. doi:10.1111/j.1365-2966.2012.21948.x
- Chiar, J. E., & Tielens, A. G. G. M. 2006, *ApJ*, 637, 774. doi:10.1086/498406
- Cushing, M. C., Vacca, W. D., & Rayner, J. T. 2004, *PASP*, 116, 362. doi:10.1086/382907
- Dahmen, G., Huttemeister, S., Wilson, T. L., et al. 1998, *A&A*, 331, 959.
- Dinerstein, H. L. 2001, *ApJ*, 550, L223. doi:10.1086/319645
- Durand, S., Acker, A., & Zijlstra, A. 1998, *A&AS*, 132, 13. doi:10.1051/aas:1998356
- Elias, J. H., Rodgers, B., Joyce, R. R., et al. 2006a, *Proc. SPIE*, 6269, 626914. doi:10.1117/12.671765
- Elias, J. H., Joyce, R. R., Liang, M., et al. 2006b, *Proc. SPIE*, 6269, 62694C. doi:10.1117/12.671817
- Eser, S., & Özdemiř, L. 2019, *CJP*, 97, 529. doi:10.1139/cjp-2018-0385
- Fazio, G. G., Hora, J. L., Allen, L. E., et al. 2004, *ApJS*, 154, 10. doi:10.1086/422843
- Ferland, G. J., Chatzikos, M., Guzmán, F., et al. 2017, *RMxAA*, 53, 385
- Figer, D. F., McLean, I. S., & Morris, M. 1999, *ApJ*, 514, 202. doi:10.1086/306931
- Frew, D. J., Bojićić, I. S., & Parker, Q. A. 2016a, *Journal of Physics Conference Series*, 728, 032015. doi:10.1088/1742-6596/728/3/032015
- Frew, D. J., Parker, Q. A., & Bojićić, I. S. 2016b, *MNRAS*, 455, 1459. doi:10.1093/mnras/stv1516
- Fritz, T. K., Gillessen, S., Lutz, D., et al. 2011, *ApJ*, 737, 73. doi:10.1088/0004-637X/737/2/73
- Gaia Collaboration, Brown, A. G. A., Vallenari, A., et al. 2018, *A&A*, 616, A1. doi:10.1051/0004-6361/201833051
- Gravity Collaboration, Abuter, R., Amorim, A., et al. 2019, *A&A*, 625, L10. doi:10.1051/0004-6361/201935656
- Higdon, S. J. U., Devost, D., Higdon, J. L. et al. 2004, *PASP*, 116, 975. doi:10.1086/425083
- Houck, J. R., Roellig, T. L., van Cleve, J., et al. 2004, *ApJS*, 154, 18. doi:10.1086/423134
- Jacoby, G. H., Kronberger, M., Patchick, D., et al. 2010, *PASA*, 27, 156. doi:10.1071/AS09025
- Jacoby, G. H., Morse, J. A., Fullton, L. K., et al. 1997, *AJ*, 114, 2611. doi:10.1086/118671
- Jacoby, G. H., & van de Steene, G. 2004, *A&A*, 419, 563. doi:10.1051/0004-6361:20035809
- Launhardt, R., Zylka, R., & Mezger, P. G. 2002, *A&A*, 384, 112. doi:10.1051/0004-6361:20020017
- Lawrence, A., Warren, S. J., Almaini, O., et al. 2007, *MNRAS*, 379, 1599. doi:10.1111/j.1365-2966.2007.12040.x
- Longmore, S. N., Bally, J., Testi, L., et al. 2013, *MNRAS*, 429, 987. doi:10.1093/mnras/sts376
- Lorenzo, M., Teyssier, D., Bujarrabal, V., et al. 2021, *A&A*, 649A, 164L. doi:10.1051/0004-6361/202039592
- Mills, E., Morris, M. R., Lang, C. C., et al. 2011, *ApJ*, 735, 84. doi:10.1088/0004-637X/735/2/84
- Minniti, D., Dias, B., Gómez, M., et al. 2019, *ApJL*, 884, L15. doi:10.3847/2041-8213/ab4424
- Miszalski, B., Parker, Q. A., Acker, A., Birkby, J. L., Frew, D. J., & Kovacevic, A. 2008, *MNRAS*, 384, 525. doi:10.1111/j.1365-2966.2007.12727.x

- Moe, M., & De Marco, O. 2006, *ApJ*, 650, 916.
doi:10.1086/506900
- Morris, M., & Serabyn, E. 1996, *ARA&A*, 34, 645.
doi:10.1146/annurev.astro.34.1.645
- Nogueras-Lara, F., Schödel, R., Gallego-Calvente, A. T., et al. 2020, *NatAs*, 4, 377. doi:10.1038/s41550-019-0967-9
- Osterbrock, D. E. & Ferland, G. J. 2006, *Astrophysics of gaseous nebulae and active galactic nuclei*, 2nd. ed. by D.E. Osterbrock and G.J. Ferland. Sausalito, CA: University Science Books, 2006
- Parker, Q. A., Acker, A., Frew, D. J., et al. 2006, *MNRAS*, 373, 79. doi:10.1111/j.1365-2966.2006.10950.x
- Parker, Q. A., Cohen, M., Stupar, M., et al. 2012, *MNRAS*, 427, 3016. doi:10.1111/j.1365-2966.2012.21927.x
- Peimbert, M. 1978, *Chemical Abundances in Planetary Nebulae*, 76, 215
- Peimbert, M., Peimbert, A., & Delgado-Inglada, G. 2017, *PASP*, 129, 082001. doi:10.1088/1538-3873/aa72c3
- Porter, R. L., Ferland, G. J., Storey, P. J., & Detisch, M. J. 2012, *MNRAS*, 425, L28.
doi:10.1111/j.1745-3933.2012.01300.x
- Porter, R. L., Ferland, G. J., Storey, P. J., et al. 2013, *MNRAS*, 433, L89. doi:10.1093/mnras/slt049
- Ramírez, S. V., Arendt, R. G., Sellgren, K., et al. 2008, *ApJS*, 175, 147. doi:10.1086/524015
- Rauch, T. 2003, *A&A*, 403, 709.
doi:10.1051/0004-6361:20030412
- Reid, M. J., Menten, K. M., Brunthaler, A., et al. 2019, *ApJ*, 885, 131. doi:10.3847/1538-4357/ab4a11
- Roche, P. F., & Aitken, D. K. 1985, *MNRAS*, 215, 425.
doi:10.1093/mnras/215.3.425
- Sabin, L., Parker, Q. A., Corradi, R. L. M., et al. 2014, *MNRAS*, 443, 3388. doi:10.1093/mnras/stu1404
- Sahai R., Morris M. R., Villar G. G. 2011, *AJ*, 141, 134.
doi:10.1088/0004-6256/141/4/134
- Schöning, T. 1997, *A&AS*, 122, 277S.
doi:10.1051/aas:1997133
- Schönrich, R., Aumer, M., & Sale, S. E. 2015, *ApJL*, 812, L21. doi:10.1088/2041-8205/812/2/L21
- Schultheis, M., Rojas-Arriagada, A., Cunha, K., et al. 2020, *A&A*, 642, A81. doi:10.1051/0004-6361/202038327
- Schultheis, M., Sellgren, K., Ramírez, S., et al. 2009, *A&A*, 495, 157. doi:10.1051/0004-6361:200810342
- Scott, P., Grevesse, N., Asplund, M., et al. 2015a, *A&A*, 573, A25. doi:10.1051/0004-6361/201424109
- Scott, P., Grevesse, N., Asplund, M., et al. 2015b, *A&A*, 573, A26. doi:10.1051/0004-6361/201424110
- Scoville, N. Z., Stolovy, S. R., Rieke, M., et al. 2003, *ApJ*, 594, 294. doi:10.1086/376790
- Serabyn, E. & Morris, M. 1996, *Nature*, 382, 602.
doi:10.1038/382602a0
- Simpson, J. P. 2018, *ApJ*, 857, 59.
doi:10.3847/1538-4357/aab55b
- Simpson, J. P., Colgan, S. W. J., Cotera, A. S., et al. 2007, *ApJ*, 670, 1115. doi:10.1086/522295
- Simpson, J. P. & Rubin, R. H. 1990, *ApJ*, 354, 165.
doi:10.1086/168676
- Smith, J. D. T., Armus, L., Dale, D. A., et al. 2007, *PASP*, 119, 1113. doi:10.1086/522634
- Stanghellini, L., Bucciarelli, B., Lattanzi, M. G., et al. 2020, *ApJ*, 889, 21. doi:10.3847/1538-4357/ab59e4
- Stanghellini, L., & Haywood, M. 2010, *ApJ*, 714, 1096.
doi:10.1088/0004-637X/714/2/1096
- Stanghellini, L., & Haywood, M. 2018, *ApJ*, 862, 45.
doi:10.3847/1538-4357/aacaf8
- Sterling, N. C., Porter, R. L., & Dinerstein, H. L. 2015, *ApJS*, 218, 25. doi:10.1088/0067-0049/218/2/25
- Storey, P. J., & Hummer, D. G. 1995, *MNRAS*, 272, 41.
doi:10.1093/mnras/272.1.41
- Tsuboi, M., Handa, T., & Ukita, N. 1999, *ApJS*, 120, 1.
doi:10.1086/313165
- Wang, Q. D., Dong, H., Cotera, A., et al. 2010, *MNRAS*, 402, 895. doi:10.1111/j.1365-2966.2009.15973.x
- Werner, M. W., Roellig, T. L., Low, F. J., et al. 2004, *ApJS*, 154, 1. doi:10.1086/422992
- Yusef-Zadeh, F., Hewitt, J. W., & Cotton, W. 2004, *ApJS*, 155, 421. doi:10.1086/425257
- Zhang, Y., Liu, X.-W., Wesson, R., et al. 2004, *MNRAS*, 351, 935. doi:10.1111/j.1365-2966.2004.07838.x
- Zhao, J.-H., Morris, M. R., & Goss, W. M. 2020, *ApJ*, 905, 173. doi:10.3847/1538-4357/abc75e